Coordination Chemistry Reviews 254 (2010) 1151–1168

Contents lists available at ScienceDirect

Coordination Chemistry Reviews

journal homepage: www.elsevier.com/locate/ccr

Review

Organic charge-transfer complexes for STM-based thermochemical-hole-burning memory

Hailin Peng, Zhongfan Liu*

Center for Nanochemistry, Beijing National Laboratory for Molecular Sciences, State Key Laboratory for Structural Chemistry of Unstable and Stable Species, College of Chemistry and Molecular Engineering, Peking University, Beijing 100871, PR China

Contents

ARTICLE INFO

Article history:
Received 23 December 2009
Accepted 13 February 2010
Available online 20 February 2010

ABSTRACT

Data storage using scanning probe microscopy (SPM) has attracted great attention because of its nanometer-scale storage capacity. We present an overview of the recent advances and representative achievements of SPM-based data storage from the viewpoints of recording techniques including electrical bistability, photoelectrochemical conversion, field-induced charge storage, atomic manipulation

* Corresponding author. Tel.: +86 10 6275 7157; fax: +86 10 6275 7157.
E-mail address: zfliu@pku.edu.cn (Z.F. Liu).

0010-8545/$ – see front matter
doi:10.1016/j.ccr.2010.02.016

Keywords:
Charge-transfer complex
Scanning probe microscopy
Data storage
Thermochemical hole burning
TCNQ

or deposition, local oxidation, magneto-optical or magnetic recording, thermally induced physical deformation or phase change, and so forth. Among new SPM-based data storage schemes, a thermochemical-hole-burning (THB) technique was developed in our group. This review also summarizes our recent achievements in design and synthesis of organic charge-transfer (CT) complexes towards thermochemical-hole-burning memory, the correlation between hole-burning performances and physicochemical properties of CT complexes, the STM tip design and its effects on the hole-burning performance, as well as studies on the data storage mechanism.

1. Introduction

Scanning probe microscopy (SPM), including scanning tunneling microscopy (STM) [1–3], atomic force microscopy (AFM) [4], magnetic force microscopy (MFM) [5,6], scanning near-field optical microscopy (SNOM) [7,8], etc., is a branch of microscopy that examines nanometer-scale surface features of various specimens using a scanning probe. The spatial resolution of SPM technique can be as small as sub-angstrom levels because the resolution of a scanning probe is not limited by diffraction, but only by the size of the probe–sample interaction volume. Thus, on one hand, scanning probes have been widely used to produce high-resolution spatial mapping of topographic, mechanical, electronic, magnetic, optical, and thermal properties of the specimen surfaces. On the other hand, the highly localized probe–sample interaction can be used to generate a change of physical or chemical properties of the substrate at the nanoscale and achieve an ultrahigh-density array of nanopatterns for next-generation data storage. In principle, SPM memory has the potential to achieve a data density of 6 petabit/in.^{2} using a vacancy or an atom as an information bit, which is much superior to those of the commercialized storage technologies limited by the well-known superparamagnetic effect and optical diffraction.

So far, a variety of SPM-based data storage techniques have been proposed. However, to realize SPM-based data storage systems that are competitive with those of existing storage technologies, there are a number of technical challenges to overcome. Small bit size, low error rate, high probe endurance, high writing and reading speed, low cost, low energy consumption, and good scalability of the technology are essential. In fact, the emergence of new data storage principles that combines high density, high performance, and low cost could usher in seminal changes in storage technologies.

The contents of this review article are as follows. We will first summarize recent advances in SPM-based data storage systems. Then we will introduce a unique STM-based data storage technique, thermochemical hole burning on organic charge-transfer complexes, recently developed in our group. We will also summarize our recent achievements in design and synthesis of organic CT complexes towards this kind of thermochemical-hole-burning memory, the correlation between hole-burning performances and physicochemical properties of CT complexes, the STM tip design and its effects on the hole-burning performance, as well as the studies on data storage mechanism.

2. Overview of SPM-based data storage

SPM-based data storage has become a rapidly growing research field since 1990. Many publications have been presented, and several good reviews are already available [9–12]. Herein, no attempt will be made to present a comprehensive overview; rather a number of major contributions with the most general applicability and some important aspects on new data recording principles will be shown.

Typical SPM-based data storage schemes include electrical bistability, photoelectrochemical conversion, field-induced charge storage, atomic manipulation or deposition, local oxidation, magneto-optical or magnetic recording, thermally induced physical deformation or phase change, etc. Representative achievements reviewed from the viewpoints of recording techniques since 1990 are listed in Table 1.

2.1. Electrical bistability

Electrical bistability is a phenomenon in which conductance switching between a low- and a high-conducting state occurs while the surface topography remains unchanged by applying a suitable voltage pulse. Such switching phenomena can lead to molecular-scale memory elements and logic gates [12,35]. So far, various electrical bistable materials have been used to achieve nonvolatile ultrahigh data storage based on SPM [20,21,25–27,36–44]. Electrical bistable memories are also complemented by rapid developments in the field of molecular electronics, where researchers are targeting devices down to a single molecule level as a memory bit [11,45].

The basic device mechanisms proposed for the observed conductance switching include phase change, charge transfer, charge tunneling, and electroreduction. Sato et al. [20,21] pioneered an STM tip-induced electrical switching and data storage on an inorganic phase-change material, β-$Na_xV_2O_5$. The reversible recording and erasing of marks with the sizes of about 10 nm have been demonstrated. However, for β-$Na_xV_2O_5$, the recording speed of 1 ms was several orders of magnitude too slow for practical applications. In 1995, on another well-known phase-change film, $GeSb_2Te_4$, Kado and Tohda [22] achieved an electrical bistable storage with a density of up to 6.45 Tbit/in.^{2} using a conductive AFM tip. By applying a pulse between the AFM tip and the amorphous chalcogenide film, the conductance of the film was increased over 100 times while the surface topography of the recorded regions was not changed. Two resistance switching mechanisms (phase change and polarity-dependent) were speculated for the chalcogenide films [46,47] but were not clarified in Kado's work [22]. Recently, Pandian et al. [48] exploited these two mechanisms simultaneously and demonstrated that reversible polarity-dependent resistance switching in phase-change chalcogenide films was feasible. They successfully produced and erased nanometer-scale crystalline marks in Sb rich amorphous $Ge_2Sb_{2+x}Te_5$ films by electrical pulses through a conductive AFM tip.

Organic electrical bistable materials have attracted much attention for building large-area, mechanically flexible low-cost, and light-weight electronic devices. Researchers in China have been active in this field [20,21,25–27,36–44]. The switching mechanism of organic electrical bistable materials is mainly based on electrical field-induced charge transfer and the interfacial polarization. Ma et al. [25] achieved STM-based ultrahigh-density data storage on a crystalline organic electrical bistable thin film, N-(3-nitrobenzylidene)p-phenylenediamine. The smallest recorded mark was 0.7 nm in size, corresponding to a storage density of 10^{15} bit/in.^{2}. Large-area ultrahigh-density data storage can be realized in organic electrical bistable materials. For example, Yano et al. [23,24] carried out AFM-based large-area data storage using con-

Table 1
Representative work on SPM-based data storage since 1990.

Time	Author/Institute	Storage mechanism	Ref.
1990	Eigler and Schweizer (IBM)	Atom manipulation using STM, Xe on Ni surface	[13]
1990	Liu et al. (Tokyo Univ.)	Photoelectrochemical, azobenzene LB film	[14]
1991	Barrett and Quate (Stanford Univ.)	Field-induced charge separation, $SiN_x/SiO_2/Si$ (NOS)	[15]
1992	Mamin et al. (IBM)	Thermomechanical writing, polymer thin films	[16–18]
1993	Bard and co-workers (Texas)	Photoconductor, ZnODEP	[19]
1993	Sato et al. (NEC)	Electrical bistability, β-$Na_xV_2O_5$ glass	[20,21]
1995	Kado and Tohda (Matsushita)	Conductance change, $GeSb_2Te_4$	[22]
1996	Yano et al. (Canon)	Conductance change, PI polymer LB film	[23,24]
1996	Pang and co-workers (CAS, China)	Electric bistability, organic complex film	[25–27]
1999	Manalis and co-workers (MIT)	Chemical oxidation, carbon nanotube tip	[28]
2000	Liu and co-workers (PKU, China)	Thermochemical hole burning, charge-transfer complex	[29]
2000	Vettiger and co-workers (IBM)	"Millipede", 100–200 Gbit/in.^{2}	[30]
2001	Quaade et al. (Technical University of Denmark)	STM-based atomic reversible data storage on silicon at room temperature	[31]
2003	Cavallini et al. (Sezione di Bologna)	Supramolecular surface patterning mechanically with AFM	[32]
2006	Hamann et al. (IBM)	Thermally induced phase change, 3.3 Tbit/in.^{2}; data rate: 100 MHz	[33]
2009	Jo et al. (Postech, Korea)	Pressure-based phase change, block polymer, 1 Tbit/in.^{2}	[34]

ductance change in a polyimide Langmuir–Blodgett film. 1 Mbit stable writing was realized with the overall error rate less than 2×10^{-3}. The diameter of the bit is about 10 nm.

2.2. Photoelectrochemical conversion

A remarkable feature of photoelectrochemical conversion data storage is that the writing, reading and erasing of the information bit is performed by coordinated photon (optical) and electron (electrical) processes. The storage material is therefore required to have both optical and electrical responses. SPM/SNOM probes can be employed as a highly focused electric field sources and/or light beam sources to localize chemical or physical change of the storage materials. A typical example of photon-mode optical recording is the well-known photochemical-hole-burning (PHB) memory. PHB is the site-selective and persistent photobleaching of an inhomogeneously broadened absorption band, induced by resonant laser light irradiation at low temperatures. The narrow and stable photochemical holes can be "burned" into the absorption bands for high-density frequency-domain optical data storage [49,50]. On the other hand, electron-mode photoelectrochemical recording with SPM has been a good candidate for an ultrahigh-density memory. Since 1990, Liu et al. [14] have extensively studied the photoelectrochemical properties of azobenzene derivatives and proposed an SPM-based optical–electrical hybrid data storage using the azobenzene derivative. A distinct difference was observed in the electrochemical reduction potential between *trans*- and *cis*-isomers in the assembled monolayer film of the azobenzene derivative, which has potential applications in photoelectrochemical data storage. In principle, the storage density can reach 10^{12} bit/in.^{2}. Another organic material, zinc-octakis(beta-decoxyethyl)porphyrin (ZnODEP), also exhibited excellent optoelectronic properties and memory behavior. Liu et al. [19,51] have achieved optical–electrical data storage based on charge trapping within a solid thin film of the ZnODEP photoconductor. In this case, the individual data bits created by an STM tip could be as small as 40 nm in diameter, corresponding to a density of 5×10^{11} bit/in.^{2}. The charge trapping or detrapping could be realized with a single 10 ns laser pulse. Most recently, Ma et al. [52] demonstrated a photoelectric cooperative effect on STM-based data storage. An organic bilayer thin film composed of titanylphthalocyanine-N,N,N′,N′-tetra(4-methylphenyl)-(1,1′-biphenyl)-4,4′-diamine (TiOPc-TTB) with good photoelectric cooperative properties was used as the storage medium. The ON/OFF current ratio was remarkably enhanced and the threshold voltage was reduced when the thin film was irradiated with suitable light intensity.

2.3. Field-induced charge storage

In general, electric field-induced charge storage (charge separation, charge trapping and change transfer) uses charge "dots" as data bits. An existence of an energy barrier within the charge storage material is critically required to prevent the recombination of the positive and negative charges, even after the electric bias has been removed. Electrets and ferroelectric materials are commonly employed as charge storage materials. A charge can be recorded within the storage media by applying a suitable voltage pulse with a conductive SPM probe that is capable of charge-sensing. The local capacitance or surface potential of the recorded region in the dielectric media will change, which can be detected with the SPM probe.

In 1991, Barrett and Quate [15] at Stanford University pioneered the charge storage trapped in the $SiN_x/SiO_2/Si$ (NOS) structure using scanning capacitance microscopy (SCaM). A localized bias was applied to the NOS sample by the SCaM tip, causing charge to tunnel through the oxide layer and to be trapped in the nitride film. This trapped charge bit induces a depletion region in the Si substrate, which can be detected with a capacitance sensor tip. The bit sizes can be as small as 75 nm, corresponding to a density of 27 Gbit/in.^{2}. The trapped charge bit was kept stable for 7 days. Recently, Suh et al. [53] have demonstrated the surface potential imaging in the $SiO_2/SiN_x/Si/SiO_2$ substrate using an AFM cantilever with field effect transistor structure. Mesquida et al. [54] have written a nanoscale charge pattern in an electret fluorocarbon film with an AFM probe. Ferroelectric thin films are promising candidates for high-density charge storage media. For example, Chen et al. [55] have described the formation and visualization of nanoscale polarized domains in ferroelectric lead zirconate titanate thin films using an AFM probe.

2.4. Atomic manipulation or deposition

Atomic manipulation and deposition are especially appealing in the fields of nanoscience and nanotechnology. Since the scanning probe is essentially a nanoscale effector combined with a high-precision mechanical movement controller, the ultrasharp probe tip is able to act as an atomic manipulator. In 1990, Eigler and Schweizer [13] pioneered the atomic manipulation of creating artificial structures "IBM" by the direct movement of adsorbed Xe atoms on a Ni(1 0 0) surface with a STM tip in an ultrahigh vacuum at 4 K. In the subsequent work, Eigler and co-workers at IBM have successfully arranged adsorbed CO molecules in atomically precise configurations on a Cu(1 1 1) surface with a low-temperature STM, and demonstrated a working logic device consisting of molecular cascade architectures [56]. A room-temperature repositioning

of individual C_{60} molecules at Cu steps has also been achieved by Cuberes et al. [57]. In 2001, Quaade et al. [31] have reversibly switched a single hydrogen atom between two symmetric sites on a silicon dimer of the Si(1 0 0) surface with a STM tip at room temperature, which is a model binary switch for single-atomic reversible data storage. Later on, the memory structure, reliability, speed, and fundamental limitations of such single-atom data storage techniques have been investigated in detail by Bennewitz et al. [58]. It is also interesting to note that an AFM probe was employed as a nanoscale manipulator to achieve large-area high-density data storage on a supramolecular film, demonstrated by Cavallini et al. [32]. AFM-based data storage with the density of 10–100 Gbit/in.^{2} was achieved using supramolecular surface patterns. It was proposed that the mechanical perturbation effect of the AFM tip during line scans induces the topographical change of the supramolecular film.

On the other hand, the SPM tip can act as an effective tool to induce materials transfer and deposition at the nanoscale, which could be used for high-density data storage. In the early 1990s, a number of publications showed that nanoscale mounds and pits could be created on various substrates by applying a suitable voltage pulse to the SPM tip. Atomic transfer between the probe tip and the sample surface were observed. This phenomenon would be explained in terms of two major mechanisms: tip–sample contact and field evaporation. Pascual et al. [59,60] have proposed that a protrusion on the tip and/or the sample can be induced by the high electric field or electrostatic forces. This protrusion would lead to a mechanical contact and create a nanostructure on the substrate. Another study that we need to mention is that of Gratzke and Simon [61]. They have postulated that a thermal expansion of the tip would result in a mechanical contact when a significant enhancement of the electric field intensity occurs in the tip vicinity. In 1990, Mamin et al. [62] observed a similar gold atom transfer process between a gold STM tip and gold substrate. However, they considered another mechanism for the formation of gold mounds through the field evaporation of gold in the STM configuration. This field evaporation of materials in STM bears a resemblance to the field evaporation process observed in the field-ion microscope. In 1991, Tsong [63] extended the theoretical models of field evaporation in field-ion microscopy to STM and concluded that negative field evaporation may be favored. In the subsequent study of Tsong and co-workers [64], Au atom transfers induced by both positive and negative field evaporations were observed under an STM configuration in UHV. They also confirmed that the STM tip can sustain itself only if it is in negative polarity. Besides the Au system [65], other atomic transfer processes induced by field evaporation have been extensively studied in many cases [66], such as gold-coated AFM probe–Si, SiO_2, and graphite substrate [67–70], and Pt/Ir STM tip-sputtered carbon films [71].

In principle, both field evaporation process and mechanical contact process may be very sensitive to the tip–sample distance and many other factors. In most previous studies, the use of STM or AFM tips either in actual contact or in very close proximity with the sample surface complicates the study of the actual underlying mechanism. Therefore, in spite of increasing interest in these nanofabrication and data storage schemes, the actual processing mechanism is still controversial. And the reproducibility and reliability need further improvement.

2.5. Local oxidation

Local oxidation or nano-oxidation of semiconducting, metallic and organic films by a STM or conductive AFM tip is emerging as a reliable and versatile method to nanometer-scale modification, fabrication and data storage. Local oxidation data storage mechanism involves an electrochemical oxidation of the sample surface in humid air, or by field-enhanced oxidation in a dry environment. The material on the sample surface exposed to the SPM tip-induced electric field undergoes local electrochemical reactions. These changes between recorded and unrecorded areas can be clearly distinguished using contrast enhancing techniques such as conductance, force modulation, lateral force, dI/ds or dI/dV. Good reviews on scanning probe lithography based on local oxidation are already available [9,10]. Herein, we briefly mention some representative work in this field.

In the aspect of the storage medium, a large number of materials have been employed as local oxidization media including silicon, metal films, silicon nitride, silicon carbide, III–V semiconductors, perovskite manganite thin films, and organic materials such as organosilane and alkane thiolate self-assembled monolayers, as well as polymer films [9,10]. Silicon surfaces, because of the technological significance of this material, are most frequently used for local oxidation lithography or data storage. Instead of silicon, bulk metals or metal films were also employed in the SPM lithography and data storage experiments. For example, titanium surfaces have been patterned by Sugimura et al. [72,73] using a local oxidation strategy with an STM tip. The humidity was very important on TiO_2 patterning, as was seen for silicon surfaces. An electrochemical process in the water-filled gap between tip and sample could result in the oxidation of Ti to TiO_2 [72,74]. By using single-walled carbon nanotube probes and atomically flat Ti films, Cooper et al. [28] in 1999 demonstrated ultrahigh-density data storage with an areal density of 1.6 Tbit/in.^{2} They reported that 8 nm bits with 20 nm pitch were written by anodically oxidizing Ti film at a rate of 5 kbit/s at room temperature in air.

2.6. Magneto-optical or magnetic recording

Magnetic recording is a form of non-volatile memory that uses different patterns of magnetization in a magnetizable material to store data. In 1888, Oberlin Smith first published a description of magnetic recording in Electrical World. Then, for the first time, a Danish engineer Valdemar Poulsen publicly demonstrated a magnetic recorder in 1898. Until the late 1980s, magneto-optical (MO) recording technology was not introduced. Magneto-optical recording writes/reads magnetic medium optically. During recording, the magnetic medium is heated locally by a laser beam, which decreases the coercive field. Then, the local magnetic polarization can be switched by a small magnetic field, and the polarization is retained when temperature drops. During reading, the reflected light varies in the polarization area due to the magneto-optical Kerr effect when the laser projects on the magnetic medium.

Compared with traditional magnetic recording, magnetic probe recording is a promising alternative, because one can make use of both high resolution of SPM and the well-developed magnetic materials explored in hard disk or magneto-optical recording systems. Hosaka et al. [75] reported the formation of nanoscale magnetic domains in a Pt/Co multilayer magnetic film with a MFM probe. Analogous to the situation in magneto-optic recording where heating is achieved by a focused laser beam, extremely small optical spots produced with the SNOM technique can act to image and record magneto-optical domains. For instance, Betzig et al. [8] have demonstrated that magneto-optical domains with the diameter of 60 nm can be recorded and detected in a Co/Pt multilayer film with SNOM.

2.7. Thermally induced physical deformation or phase change

The SPM probe can act as a tiny heater to induce a local physical deformation or phase change of the thermally sensitive storage

media for data recording. Extensive studies have been done since 1992 [16]. The performance of SPM-based thermal recording has been greatly improved in the past 18 years. We will review representative achievements in the SPM-based thermal recording.

In 1992, Mamin and Rugar [16] at the IBM Almaden Research Center pioneered thermomechanical writing of topographic features on PMMA films using an AFM cantilever equipped with a heater on its tip. An indentation with the size of ~20 nm was created thermomechanically by the heated AFM tip in the 20 nm thick PMMA film that stands for a logical "1". Erasing of data was also performed by means of heating either the entire plastic card or its local region.

A thermomagnetic writing was also demonstrated on a 29 Gbit/in.^{2} patterned magnetic medium, a continuous CoCrPt film, by using Joule heat generated by a current flowing between an MFM tip and the magnetic medium [76]. The thermomagnetic methods typically use a current flow in a conductive SPM probe or a near-field laser beam for local heating. However, the availability of the method of flowing a current might be limited in practical thermomagnetic recording, since flowing a large current requires direct contact between the head and media, which causes a serious problem of abrasion. The combination of near-field modulation and near-field laser-beam heating should be a more promising method for thermomagnetic recording, which may overcome the problem of abrasion. In 2004, Hamann et al. [77] have carried out a thermomagnetic recording on 16 nm thick Co/Pt alloy films using an AFM tip combined with a pulsed-laser. Specifically, magnetization patterns with a spacing of ~40 nm between the bits were achieved. The corresponding storage density is about 400 Gbit/in.^{2} The current magnetic storage density is limited to ~0.5 Tbit/in.^{2} due to the well-known superparamagnetic effect. Hamann et al. also predicted that potential storage densities of >1 Tbit/in.^{2} with recording speeds of >1 GHz can be realized with thermomagnetic recording using an AFM tip combined with a pulsed-laser, superior to current magnetic storage density. Onoue et al. [78] also studied a thermomagnetic writing on a CoNi/Pt multilayered film through a heat-assisted MFM tip and obtained the magnetic bits with a diameter of 80 nm. It is noted that Lu et al. [79] fabricated nanostructures on both gold films and H-passivated Ge surfaces by using lasers in combination with a STM tip in 2000. They concluded that the mechanism of pits formation on gold films was based on a thermomechanical indentation induced by a thermal expansion of the tip under laser irradiation. For H-passivated Ge surfaces, however, the tip-enhanced optical field thermally desorbed the hydrogen atoms from the sample surface, resulting in nano-oxidation based on the optical enhancement underneath the tip during laser irradiation.

We noticed a recent study reported in 2006 in *Nature Materials*. Hamann et al. [33] demonstrated a scalability of thermal recording of erasable phase-change bit patterns at a density of up to 3.3 Tbit/in.^{2} on thin-film chalcogenide phase-change materials using a heated AFM tip. The AFM cantilever was heated to about 350 °C by pulsed-laser irradiation. The heat was then transferred from the AFM tip to the storage media and thus induced a phase change. The data rate was 100 MHz for writing/reading with an estimated signal-to-noise ratio ~20 dB. The erasing rate was 10 MHz. Power requirements were less than 10 mW, excluding the spinning of a disk. All these results were very competitive to those of existing storage technologies, and demonstrated that the AFM-based thermally induced phase-change storage/memory can be a very promising concept to realize alternative memory devices.

Jo et al. [34], in their study in 2009 in *Nature Nanotechnology*, reported a pressure-based phase-change ultrahigh-density data storage using AFM but without a heated tip. Local phase transitions of a specific block copolymer film exhibiting a baroplastic property were caused by the indentation of an AFM tip at room temperature. They have achieved a data storage density of 1 Tbit/in.^{2}, which is limited only by the size of the tip. This concept of the pressure-based phase-change memory at room temperature may be used for next-generation ultrahigh-density data storage.

SNOM is capable of utilizing evanescent energy to produce extremely small optical spots that locally illuminate/heat the recording layer [80]. In 1996, Hosaka et al. [81,82] have firstly demonstrated nanometer-sized phase-change recording in $Ge_2Sb_2Te_5$ thin film using a reflection SNOM with a 785 nm wavelength laser diode. The temperature rise due to light irradiation of an evanescent light through the SNOM aperture induces an amorphous–crystalline phase change of the recording film so that the reflectivity of the irradiated area increased. The recorded bit size decreases with the decrease of the input laser power and optical aperture size of the SNOM probe. The smallest bit size was 60 nm in diameter, which corresponds to a density of 170 Gbit/in.^{2} [83]. By using a new type of SNOM–scanning interfermetric apertureless microscopy (SIAM), Martin et al. [84] have achieved a density of 256 Gbit/in.^{2} and an effective data rate of 30 MHz with a signal-to-noise ratio of 20 dB on e-beam fabricated bit patterns. The SIAM utilized a cantilever probe with a tip of 5 nm radius and two readout spots. One readout spot was used to produce a reference beam. The cantilever probe was placed in the central portion of the second spot. Due to the dipole interactions between the probe tip and surface, the modulation in light scattering from the sharp scattering object was detected by combining the reference beam and the beam reflected from the second spot in a sensitive homodyne interferometer. The highest predicted data storage in the 100 Tbit/in.^{2} range could be accessed at data rates of 100 MHz.

As for STM, one of the remarkable features of STM is that highly localized current can be generated between the tip and the sample. The thermal heating effect of STM tunneling current has been investigated rigorously in early studies [85–87]. The flowing electrons from the STM tip are scattered in the sample by an inelastic energy loss process. This process causes the kinetic energy of electrons to be lost in the scattered area [88–90]. The temperature of the scattered area underneath the STM tip is elevated. Therefore, tunneling/field emission current in STM can be the smallest heat source of all the instruments. The energy of the STM current has been employed to break a chemical bond [91], induce a controlled motion [90,92–95], or achieve a thermally induced recording [88].

However, for STM-based *thermophysical* storage applications the properties of the storage medium plays a crucial role. According to the Fourier heat conduction law $T = -q/k$ [89], the temperature gradient in the substrate T depends on the thermal power density dissipated in the sample q and thermal conductivity of the sample k. Due to the high values of electric conductivity and thermal conductivity of crystalline metallic substrates, the STM thermal heating effect is usually negligible [96]. Since the melting point of crystalline metallic substrates is relatively high, the thermally induced recording on these substrates is essentially not feasible. On the other hand, the thermal conductivity of multilayered films is smaller than that of crystalline metallic substrates. For example, the thermal conductivities of Co and Pt are 69.24 and 72.7 W K^{-1} m^{-1} at room temperature, respectively. The thermal conductivities of the 15.4 and 10 nm thick Co/Pt multilayered films are 20 and 10 W K^{-1} m^{-1}, respectively [77,88]. In 1995, Nakamura et al. [88] reported a STM-based thermomagnetic writing on 15.4 nm thick Co/Pt multilayered films, by using the Joule heating effect of STM current. The size of the recording mark was about 200 nm. In 1999, Saluel et al. [97] also demonstrated that the tunneling probe of STM is a sufficient heater source for an electrical resistivity change on phase-change materials. STM-based WORM memory was achieved with a storage density up to 10 Gbit/in.^{2} on the 30 nm thick Ge–Sb–Te and Ag–In–Sb–Te films.

2.8. Reading and writing rates

Until now, we have briefly summarized some of the early work covering the important aspects on new data recording principles for SPM-based data storage. It is noted that local oxidation, atom manipulation or deposition, physical deformation based SPM storage techniques are often non-reversible, which naturally limits the applicability of these schemes. It has been recognized for quite a long time that the writing and reading rates of a SPM may be too slow for any practical applications in mass data storage due to the inherent slowness of the SPM configuration. For instance, due to the limitations of the feedback loop response and the mechanical resonant frequency in AFM cantilevers, the data rates of a single cantilever are a few Kbit/s in an AFM-based data storage system, whereas data rates of 100 Mbit/s or more have been achieved in conventional magnetic storages. The low tunneling currents and slow feedback speed severely limited STM-based data storages to even lower data rates.

Fortunately, many efforts have been made to greatly improve the data rate of SPM-based data storage so far. In 1993, Altman et al. [98] utilized a computer and a commercially available data acquisition card to achieve a high-speed data acquisition and control system. Kuipers et al. [99] also improved scan rates (10^5 data points/s) with fast analogue electronics and a combination of a workstation and three transputers in 1995.

For higher data rate, a rotary disk-type AFM recording system [16,100] with a high-speed air spindle motor has been used since 1992. A high resonant frequency AFM cantilever was developed by Hosaka et al. [83] in 1997. They demonstrated an ultrahigh recording density of 1.2 Tbit/in.^{2} and a readout speed of 1.25 Mbit/s. To further overcome resonant frequency limitation, Mamin et al. [101] in 1999 have fabricated highly compact implementation integrating piezoresistive sensors on low-mass Si cantilevers for AFM-based data storage. They have successfully reduced the mechanical response time to 90 ns, corresponding to data rates of about 10 Mbit/s, comparable to that of the DVD.

On the other hand, since 1995, Quate and co-workers [102–105] have pioneered the parallel AFM cantilevers with integrated sensors and actuators technique to lift the restrictions of a single AFM cantilever. In 1997, Binnig [106] presented a 5×5 array of individually controlled cantilevers. In this parallel operation, each cantilever acted as an autonomous system, which significantly increased the whole data rate and density.

Currently the most advanced example of a parallel storage system is the IBM "Millipede" that combines ultrahigh density and high data rate [30,107–109]. Large two-dimensional AFM probe arrays acted as independent writing, reading and erasion elements. The writing was done thermomechanically on polymer thin films via heating of the AFM tip. Initial areal densities of 100–200 Gbit/in.^{2} have been achieved with the 32×32 array chip, which has potential for further improvements. The data rate can reach 35 Mbit/s, superior to that of a DVD. They stated that the recording density can be over 1 Tbit/in.^{2} in principle [109]. The results are quite encouraging to make efforts in this promising direction. Future developments of new parallel scanning probes and renovation of storage techniques will lead to industrial-scale application of SPM-based storage techniques that combine high data rate and ultrahigh density.

3. Thermochemical-hole-burning memory

The common characteristic of SPM *thermophysical* storage methods is that a SPM probe is employed as a nanometer-sized heater to induce a physical change of the storage medium for data recording. In our recent work [110–117], we have proposed a novel STM-based thermochemical-hole-burning (THB) technique for data storage, which utilizes the STM current heating effect to induce a nanometer-scale *thermochemical* decomposition of organic charge-transfer (CT) complexes and subsequent gasification of the low-boiling point decomposition product for writing a data bit as a nanometer-sized hole. Fig. 1 shows the scheme of the THB process. A single crystal of organic CT complex is fixed onto a metallic plate with highly conductive silver adhesive for STM investigation and hole writing. When applying a voltage pulse between the STM tip and the single crystal of CT complex, a high-density electron flux passes through a finite area on the sample surface determined by the tunneling/field emission mode and the tip geometry. An electron–phonon interaction in the sample occurs, and the electron energy is then transferred to the crystal lattice by an inelastic energy loss process [88–90]. This results in an increase in lattice vibrations and the local temperature underneath STM tip is elevated significantly. When the local temperature rises above the decomposition points of the CT complexes, a localized decomposition reaction takes place. The volatile decomposition products are then gasified, leaving a hole on the sample surface. Our experimental and theoretical studies have confirmed the concept of THB data storage [110–117].

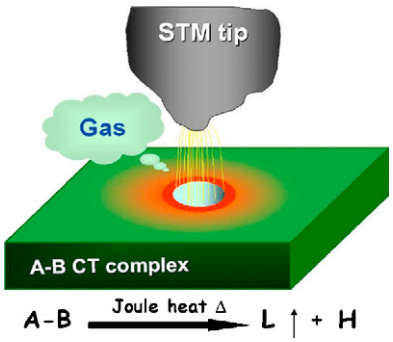

Fig. 1. Schematic diagram of the STM-based thermochemical-hole-burning (THB) process. L: low-boiling point components; H: high-boiling point components.

A variety of organic CT complexes have been proven as suitable THB materials [110–118]. Organic CT complexes have low thermal conductivity (the order of $\sim$0.5 W K^{-1} m^{-1}) [119–121], relatively low room-temperature conductivity [122], remarkably low decomposition temperatures [122,123], and a short electron mean free path [124], when compared with normal crystalline metals. These features facilitate the use of low flux of heat generated by STM current for localized thermal decomposition of the CT complex substrate. The decomposition of CT complexes evolves volatile products, which also helps the formation of a nanometer-sized hole on the crystal surface with high repeatability. However, this thermochemical decomposition leads to a volatile and non-reversible storage scheme, which naturally limits the applicability of the organic CT complex as a rewritable recording medium.

The THB data storage technique has a number of advantages compared with the STM-based *thermophysical* storage techniques and other SPM memories as follows: (1) ultrahigh density. The data bit can be easily down to a few nanometers because of the ultrathin tunneling electron beam and its highly localized heating effect on the organic CT complexes with low thermal and electrical conductivity. In principle, molecular-scale data storage can be achieved through the STM-induced decomposition reaction at molecular scale. (2) Excellent writing repeatability and reliability. The decomposition temperature of an organic CT complex is much lower than the melting point of the tip material. Hence the thermal deformation of an STM tip in the data writing process is negligible. The low writing temperature is also suitable for the low energy flux of STM current. The non-contact writing mechanism gives the STM tip high endurance on wearing and physical deformation. As a result,

the repeatability of determining the hole size and the reliability of hole-formation is very high, reaching 100% for large-area data recording. (3) Organic CT complexes have enormous flexibility for molecular design compared with inorganic materials, which provide much room for improvement in the storage material. (4) THB systems may open up an avenue for the studies of nanometer-scale reactions and even single molecular reactions. The hole burning process typically involves hundreds or tens of molecules, which can be well controlled by the amplitude and duration of the voltage pulse. It would be of great interest to learn about the kinetics and thermodynamics of such a nanoreaction system.

4. Synthesis and characterization of organic charge-transfer complexes

4.1. Synthesis

The synthesis of organic CT complexes has received considerable attention due to their intriguing electronic, optical, and magnetic properties in the last four decades, beginning with the first report of conducting salts of the powerful planar electron acceptor, 7,7,8,8-tetracyanoquinodimethane (TCNQ). In our recent studies [110–118], we have developed a number of single crystals of organic CT complexes as promising STM-based THB data storage materials. The general rules for designing the organic CT complex material used for THB data storage includes: (1) the CT complex with donor-acceptor association has a good enough conductivity and high enough stability for STM operation; (2) the donor and acceptor have a moderate electrostatic attraction that provides a stabilizing force and ensures suitable decomposition temperature; (3) The CT complex has low-boiling point decomposition products for gasifying in the THB wring process; (4) the thermal conductivity of the CT complex should be low enough, which facilitates an utilization of low energy flux generated by STM current for high writing reliability and ensures an effective confinement of current heating area for high-density recording; (5) the storage media should have an atomically flat surface over a large area that ensures the ultrahigh density and capacity.

Most TCNQ-based binary CT complex memory materials have molecular units represented by formula $M^+(TCNQ^0)(TCNQ^-)$, which contain molar proportions of neutral $TCNQ^0$ associated with $TCNQ^-$ and a cation M^+ [122]. The cation M^+ is represented by alkyl- or aryl-substituted ammonium (including N-heterocycles), phosphonium, and sulfonium ions. In the solid state there is electron delocalization between $(TCNQ^-)$ and $(TCNQ^0)$ in the π-stacked chain as implied by the formula $(TCNQ)_2{}^-$. Almost all types of binary complexes memory materials, $M^+(TCNQ^0)(TCNQ^-)$, can be synthesized according to the general method of Melby et al. [122] in 1962. They described a major synthetic route to these binary CT complexes written as the following reaction:

$$3M^+I^- + 4TCNQ \rightarrow 2M^+(TCNQ^0)(TCNQ^-) + M^+(I_3)^- \quad (1)$$

From the equation, the iodide ion is oxidized to free iodine and provides the electron for the formation of $TCNQ^-$. Triiodide ion in solution was scavenged as the result of the redox reaction between the iodide ion and TCNQ.

On the other hand, a series of ternary TCNQ salts containing TCNQ and $I_3{}^-$ chains and ammonium cation (alkyl ammonium–TCNQ–iodide) were synthesized in the late 1970s [123,125–127], following the reaction:

$$3M^+I^- + 3TCNQ \rightarrow (M^+)_3(TCNQ)_3{}^{2-}(I_3)^- \quad (2)$$

Note that those compounds all have a $(CH_3)_2N^+H$ group, which seems to be a necessary condition for the synthesis of these ternary CT complexes. In 1988, a ternary sulfonium–TCNQ–iodide was synthesized by Izumi et al. [128].

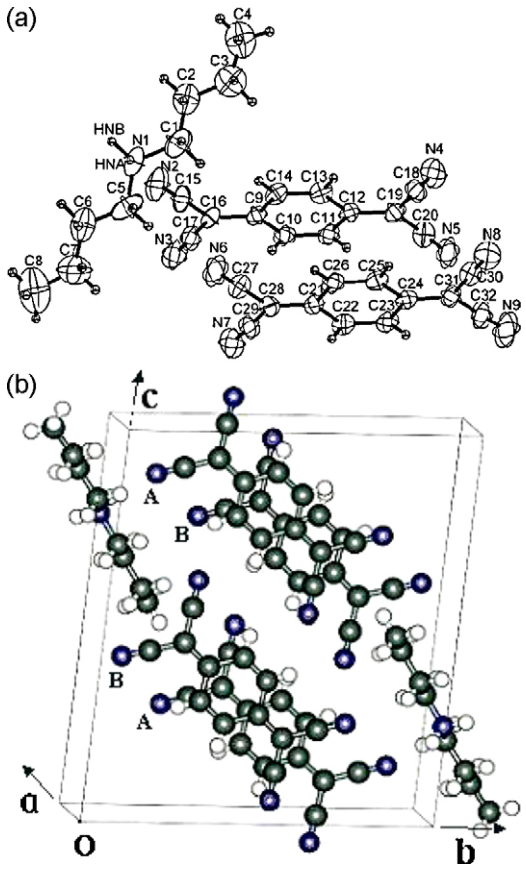

Fig. 2. (a) Molecular structure of $DBA(TCNQ)_2$ with atom labelings and (b) perspective views of the crystal structure of $DBA(TCNQ)_2$. These graphics are reproduced from Ref. [111]. Copyright Wiley–VCH Verlag GmbH & Co. KGaA. Reproduced with permission.

Following the above methods, we have synthesized thirty THB storage materials, including several series of TCNQ-based complexes such as ammonium–TCNQ, quinoline–TCNQ, pyridine–TCNQ, morpholinium–TCNQ, and ternary ammonium–TCNQ–iodide [110–118]. We have synthesized a new CT complex, $DBA(TCNQ)_2$ [DBA = dibutylammonium] that exhibited excellent THB proprieties [111,118].

4.2. Crystalline characterization

Single-crystal X-ray diffraction has been widely used to determine the crystal structure and molecular arrangement of CT complexes. The as-grown crystals of CT complexes typically exhibit a needle shape that are up to centimeters long, millimeters wide and thick.

TCNQ-based CT complexes usually have a layered structure in which layers of TCNQ molecules alternate with layers of cations M^+. Take the new compound $DBA(TCNQ)_2$ for example [111]. Fig. 2 depicts the molecular structure and arrangement of $DBA(TCNQ)_2$ at room temperature. The $DBA(TCNQ)_2$ crystal is triclinic with space group $P\bar{1}$ and $a = 6.6543$ Å, $b = 14.192$ Å, $c = 15.908$ Å, $\alpha = 83.39°$, $\beta = 79.21°$, $\gamma = 90.02°$, $Z = 2$. A DBA cation and two crystallographically independent TCNQ molecules (*A* and *B*) exists in the asymmetric unit. The TCNQ molecules are stacked face-to-face along the *a*-axis with repeat sequence *AB* leading to two independent spacing distances ($d_{AB} = 3.25$ Å, $d_{BA'} = 3.39$ Å). The packing can be described as a set of TCNQ columns (in effect, a stack of *AB* diads) parallel to the *a*-axis and spaced by chains of DBA cations in the *b*-direction, indicating a layered structure along

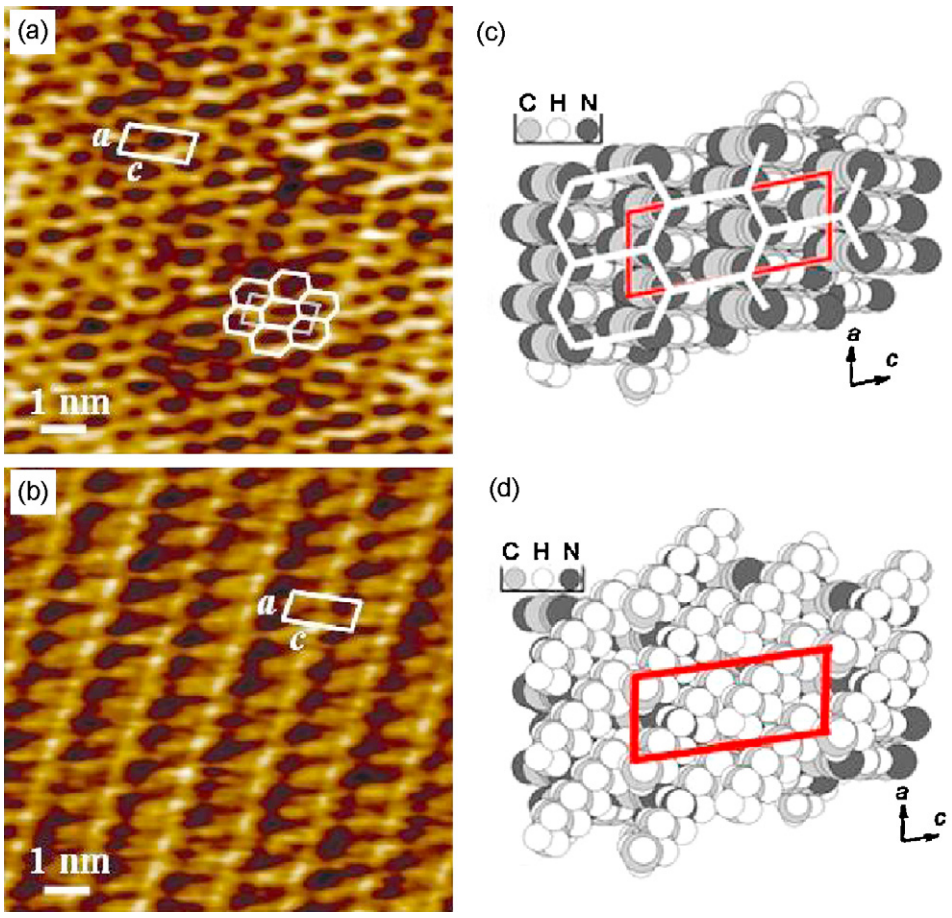

Fig. 3. (a and b) Typical molecular-resolution STM images of the DBA(TCNQ)$_2$ crystal surface. Imaging conditions were I_t = 0.10 V, V_b = 0.10 nA; constant-current mode (I_t: tunneling current; V_b: sample bias voltage). The atomic arrangement on the surface of *ac*-plane terminated with TCNQ (c) and covered with DBA cations (d). These graphics are reproduced from Ref. [111]. Copyright Wiley–VCH Verlag GmbH & Co. KGaA. Reproduced with permission.

the *b*-axis. The remarkable electronic, optical, and magnetic properties of TCNQ-based CT complexes, in essence, arise predominately from the quasi one-dimensional (1D) conductive chains formed by a stacking arrangement of planar TCNQ molecules [129–131]. Further, we have studied the crystal structure transition of 1D TCNQ chain in DBA(TCNQ)$_2$ by detailed X-ray structure analyses at different temperatures [118]. A first-order reversible structural change related to a dimer–tetramer transition along the TCNQ chain and disruption of the hydrogen-bonding chains was indicated as the temperature decreases from 270 to 253 K, which is the origin of the electronic and magnetic transition. A direct correlation of physical properties with crystal structure during the transition was established.

4.3. Surface structure characterization

The surface structure and property of storage materials play a crucial role in SPM-based ultrahigh-density data storage. Hence it is necessary to carry out surface structure characterization of our THB materials. STM is a powerful tool to study the atomic-level structural and electronic features of a conducting substrate [132]. We have demonstrated that the STM imaging is an effective method to determine the crystallographic orientations and molecular arrangement on the surface of the CT complexes including ammonium–TCNQ, quinoline–TCNQ, pyridine–TCNQ, morpholinium–TCNQ, and ternary ammonium–TCNQ–iodide. STM imaging results of the biggest surface of our various CT complex crystals usually reveal a molecularly flat surface terraces with a step height of 1–2 nm that corresponds to a specific lattice parameter. These terraces are mainly terminated with TCNQ molecules in a chain form, with the same periodicity as the bulk crystallographic parameters. The TCNQ molecules are in a tilted stand-upright form along the molecular long axis, with one nitrogen atom at the outermost surface. The TCNQ-terminated surfaces prefer to keep the bulk truncated state and have larger rigidity, which originate from the strong π–π stacking interaction between TCNQs. Occasionally, small terrace patches, identified as the cation layers were found at the outermost surface. It is noted that the molecular arrangements of the cations at the outermost surfaces were sensitive to the outer environment, presumably due to the weak interactions between cations and underlying TCNQs [133].

Again take DBA(TCNQ)$_2$ for example, Fig. 3a and b shows two typical molecular-resolution STM images of the biggest crystal surface of DBA(TCNQ)$_2$. The dimensions and the angle of the surface unit cell confirm that the crystal surface is the *ac*-plane. The honeycombed pattern corresponds to the arrangement of the zigzag TCNQ stacks (Fig. 3c). Interestingly, some regions of the same crystal face display a dark striped pattern under identical imaging conditions (Fig. 3d). Considering comparisons with molecular models of the *ac*-plane and the lack of density of states at the Fermi level on the DBA cations, it is reasonable to assign the dark striped pattern in Fig. 3a to DBA cations terminated regions (Fig. 3d), where DBA cations are obscurer than the underlying TCNQ molecules. These observations of two different STM images on the same crystal face are evidenced that one of these images represents an *ac*-face terminated with TCNQ anions, whereas the other represents an *ac*-face covered with DBA cations.

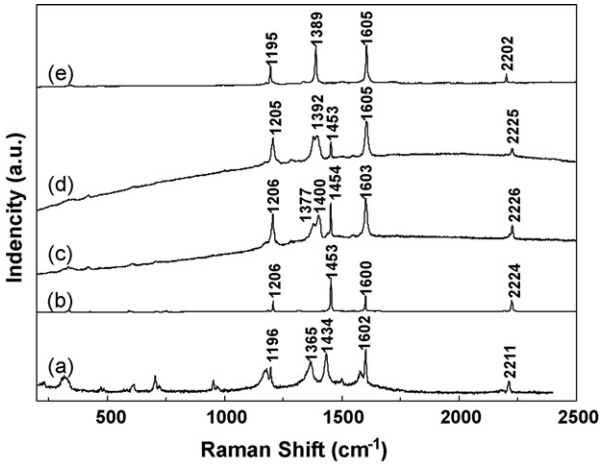

Fig. 4. Comparison of Raman spectra of DBA$(TCNQ)_2$ (a), neutral $TCNQ^0$ (b), residue of DBA$(TCNQ)_2$ after Raman laser-induced ablation (c), and two typical residue of DBA$(TCNQ)_2$ after current-induced decomposition (d and e). These graphics are reproduced from Ref. [111]. Copyright Wiley–VCH Verlag GmbH & Co. KGaA. Reproduced with permission.

In the case of TEA$(TCNQ)_2$, the correspondence between charge density patterns and surface atomic distribution has also been confirmed by STM operated in ultrahigh vacuum. Three kinds of distinct structures, monomerization, tetramerization, and octamerization of TCNQ chains with different electron density distributions, were observed on different terraces.

4.4. Raman spectroscopy

Raman spectroscopy has been a powerful tool for studying TCNQ-based CT complexes [134–140]. We have carried out extensive Raman spectroscopic studies on our as-grown CT complexes of TCNQ. Raman spectra of ammonium–TCNQ, quinoline–TCNQ, pyridine–TCNQ, and morpholinium–TCNQ compounds usually exhibit four expected characteristic vibration modes at 2208 ± 3, 1600 ± 2, 1423 ± 3 and $1192 \pm 4\,cm^{-1}$ that can be assigned to C≡N stretching, C=C ring stretching, C=C wing stretching and C=C–H bending modes, respectively. Those analogous vibration modes in neutral $TCNQ^0$ are at 2224, 1600, 1453 and 1206 cm^{-1}. The C=C wing stretching and C≡N stretching mode are quite sensitive to the electronic change of the TCNQ moiety [140]. The red shift of the C≡C wing stretching mode compared to that of $TCNQ^0$ suggests the occurrence of charge transfer. An empirical linear relation between the frequency of the characteristic C≡C wing stretching vibration in TCNQ and the degree of charge transfer was proposed [135]. From C≡C wing stretching vibration of above compounds at about 1423 cm^{-1}, the degree of charge transfer was estimated to be about 0.5 e, suggesting all TCNQs are equivalent in the TCNQ chain.

In the case of DBA$(TCNQ)_2$, comparison with the Raman spectrum of DBA$(TCNQ)_2$ and neutral $TCNQ^0$ (Fig. 4a and b) revealed that the C=C wing stretching mode at 1434 cm^{-1} was red-shifted by 19 cm^{-1}. The calculated degree of charge transfer was ca. 0.32, which suggested the average charge on a special TCNQ molecule was ca. 0.32. This value was in approximate agreement with the result estimated by our X-ray structural analysis. X-ray diffraction at room temperature further revealed that a hydrogen-bond links DBA cation with one special TCNQ, which results in the "pinning" of formal charge on the special TCNQ in the TCNQ chains.

To study the decomposition behavior of CT complexes, we have carried out laser-induced ablation experiments and in situ Raman characterizations of the decomposition product on a Renishaw system 1000 Raman Imaging Microscope. A 0.6 mW He–Ne laser beam was focused by the 50× objective onto the surface of a DBA$(TCNQ)_2$ crystal for about 5 s. As a result, a pit of about 6 μm in diameter was observed with a peltier-cooled CCD camera. Some residual powder was found around the fabricated pit. The typical Raman spectrum of the decomposition residue near the pit is shown in Fig. 4c. We can identify the $TCNQ^0$ mode at 2226, 1603, 1454 and 1206 cm^{-1}. These vibrations indicated unambiguously the presence of a substantial quantity of $TCNQ^0$ in the decomposition residue.

We also investigated the current-induced decomposition behavior of the DBA$(TCNQ)_2$ crystal with the Raman spectroscopy. Fig. 4d and e shows two typical Raman spectra of decomposition residue, respectively. Compared with the spectrum of neutral TCNQ and the simple salts (e.g. $K^+TCNQ^{\bullet -}$) [141], we identified the $TCNQ^0$ modes at 2225, 1605, 1453, and 1205 cm^{-1} (Fig. 4d) and $TCNQ^{\bullet -}$ a_g modes at 2202, 1605, 1389, and 1195 cm^{-1} (Fig. 4e). These Raman spectra confirmed the formation of $TCNQ^0$ and $TCNQ^{\bullet -}$ in the current-induced decomposition residue.

4.5. Thermal decomposition behavior

Compared with other physicochemical properties, the study of thermal decomposition behavior is still lacking. Abkowitz et al. [123] evaluated the thermal properties of CT complex NMe_3H–I–TCNQ with thermal gravimetric analysis, differential scanning calorimetry traces and X-ray diffraction. They concluded that NMe_3H–I–TCNQ decomposes into gaseous HI, NMe_3 and solid TCNQ in an open container. It is important to investigate the detailed thermal decomposition behavior of the THB storage materials although the detailed analysis of thermal decomposition products and mechanisms is tedious work, especially for large organic compounds.

Today thermogravimetry combined with mass spectrometry (TG–MS) proves to be remarkably useful for understanding thermochemical reactivity of functional materials. We carried out extensive TG–MS studies to characterize the decomposition behavior of various THB storage materials including quinoline–TCNQ, pyridine–TCNQ, morpholinium–TCNQ, ammonium–TCNQ, and ternary ammonium–TCNQ–iodide CT complexes. The TG–MS experiments were conducted on a Setaram TGA92 thermogravimetric analyzer combined with a quadrupole mass spectrometer (Balzers OmniStar 200), which provides online monitoring of the mass loss of the sample and the formation of positive ions in the range of 1–300 amu. The CT complex crystals (~10 mg) were heated at 5 °C/min under flowing argon carrier gas (~37 mL/min). The evolved gases were analyzed continuously by the mass spectrometer, where they are ionized in a 50 eV electron impact ion source.

4.5.1. TG–MS of ammonium–TCNQ CT complexes

We investigated the thermal decomposition behavior of TEA$(TCNQ)_2$ crystals in 30–400 °C with the TG–MS technique. TEA$(TCNQ)_2$ begins to decompose at ca. 195 °C and the first-step weight loss between 195 and 220 °C is about 11% from the TG curve, corresponding to the formation of gaseous products. The possible decomposition process involves an evolution of HCN molecules in the first-step weight loss through an initial cleavage of cyano groups from the TCNQ moiety and the subsequent vaporization of the low-boiling point component, triethylamine, as identified by the TG–MS results [117].

We also carried out a detailed TG–MS study of the DBA$(TCNQ)_2$ crystal in a large temperature range of 30–800 °C. The TG curve shown in Fig. 5 revealed the thermal decomposition undergoes two different steps at different weight-loss rates. The temperatures at the maximum rate of weight loss in first and second step were ca. 192 and 440 °C, respectively, according to the derivative thermogravimetric (DTG) analysis. The first-step weight loss was about 5.1 wt%, occurring between 177 and 210 °C with a faster weight-

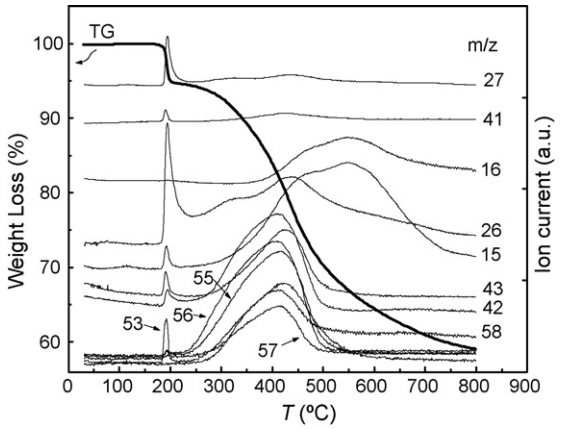

Fig. 5. TG–MS curves of DBA(TCNQ)$_2$ single crystal. The numbers correspond to the mass-to-charge ratio of ions detected from the gaseous products. TG curve, left-hand ordinate. This graphic is reproduced from Ref. [111]. Copyright Wiley–VCH Verlag GmbH & Co. KGaA. Reproduced with permission.

loss rate. The second-step weight loss was slowed down, especially above 500 °C. At 800 °C, about 60 wt% heat-resistant materials were not decomposed.

MS analysis of the evolved gases revealed the formation of ions having a mass-to-charge ratio (m/z) of 15, 16, 26, 27, 41, 42, 43, 53, 55, 56, 57 and 58 amu (shown in Fig. 5). The ion currents at masses 177 and 204 amu, the characteristic peaks of the TCNQ molecule, were insignificant in the 30–800 °C range, which indicated that TCNQ was not gasified. The curves of ion currents at masses 26 and 27 amu peaked at the same temperature (~192 °C) after subtracting the baseline, which were identified as the evolution of HCN (m/z = 27) molecules in the first-step weight loss. HCN molecules originated from the cyanide groups (–CN) of TCNQ and protons of the DBA cations, analogously to the our TG–MS results of the TEA(TCNQ)$_2$ [117] Moreover, according to the weight loss of 5.1% occurring in the first step, only half TCNQ molecules were decomposed via cleavage of one CN group. A small quantity of ions at masses 41, 42, 43, and 53 amu also peaked in the first-step weight loss, which might come from thermal degradation of a very few dibutylammonium ions.

The second-step thermal decomposition of DBA(TCNQ)$_2$ was more complicated, when compared with TEA(TCNQ)$_2$ [117] that directly released the donor molecule, triethylamine. The dibutylamine molecule has actually not been released, for the characteristic ions (m/z = 86, 129) of dibutylamine were negligible. The alkane fractions $C_4H_9^{\bullet}$ (m/z = 57) were released instead between 210 and 550 °C, which was accompanied by the appearance of $C_3H_8N^+$ (m/z = 58), alkenes $C_4H_7^{\bullet}$ (m/z = 55) and C_4H_8 (m/z = 56). We speculated that these fractions originate from the degradation of the same parent-molecule, dibutylamine. Above ca. 500 °C, smaller fractions such as CH_4 (m/z = 16), $CH_3^{\bullet}$ (m/z = 15) were dominant in the ion currents, because organic species tend to decompose to small fractions at high temperature. At 800 °C, about 60 wt% materials were still not decomposed (shown in TG curve), presumably because of the production of heat-resistant polycyclic aromatic structures. In fact, graphite-like materials existed in the residue, which was indicated by the appearance of two strong Raman peaks at 1590 and 1355 cm^{-1} appeared in the Raman spectrum of the residue, usually referred to as the G and the D band of disordered graphite, respectively [142].

The results of TG–MS experiments showed that the thermal decomposition of DBA(TCNQ)$_2$ involves initial elimination of the CN group from about half the TCNQ moieties by capturing a proton from the DBA, and subsequent thermal degradation of the ammonium salts. In terms of the crystal structure, Raman spectra, and TG–MS analysis, it is reasonable to speculate on the thermal decomposition process of the DBA(TCNQ)$_2$ crystal. The decomposition reaction undergoes two steps. In the first step, the proton of DBA cation attacks the CN group of TCNQ(B) anion via H-bonding, releasing HCN gas. The TCNQ(A) might be residual as the neutral TCNQ or TCNQ$^-$ anion by forming intermediate CT species coupled with DBA [118]. In the second step, the intermediate species DBA$^+$TCNQ$^-$ gets decomposed, releasing various low molecular weight species. In fact, TCNQ is a fast radical-trapping reagent [143]. A radical addition to TCNQ with thermally produced radicals and the same additions with loss of one of more CN groups can produce a new radical aromatic structure from a quinone structure, as confirmed by accurate mass measurements [144,145]. At higher temperature, the heat-resistant polycyclic aromatic structures are probably produced via the radical polymerization of quinone structures.

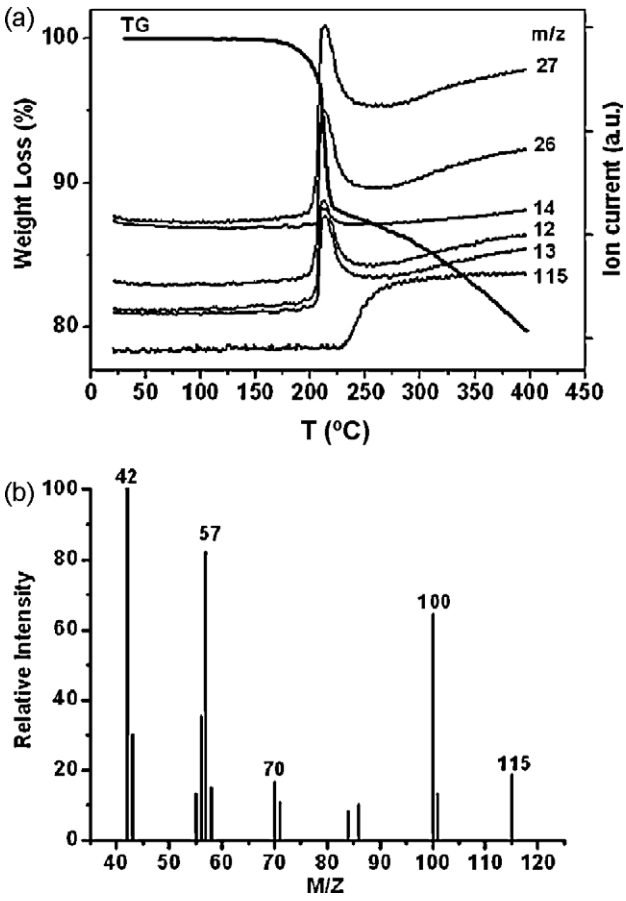

Fig. 6. (a) TG–MS curves of HEM(TCNQ)$_2$ crystal. TG curve corresponds to left-hand ordinate and the numbers are the m/z of ions of gaseous products. (b) A portion of the mass spectrum of evolution products from HEM(TCNQ)$_2$ obtained at 273 °C.

4.5.2. TG–MS of morpholinium–TCNQ CT complexes

We have prepared single crystals of a series of N-substituted morpholinium–TCNQ CT complexes, including HMM(TCNQ)$_2$, HEM(TCNQ)$_2$, DMM(TCNQ)$_2$, MPM(TCNQ)$_2$, EPM(TCNQ)$_2$, and MEM(TCNQ)$_2$ [HMM = N-methyl-morpholinium; HEM = N-ethyl-morpholinium; DMM = N,N-dimethyl-morpholinium; MPM = N-methyl-N-propyl-morpholinium; EPM = N-ethyl-N-propyl-morpholinium; MEM = N-methyl-N-ethyl-morpholinium].

Take HEM(TCNQ)$_2$ for example, the thermal decomposition behavior of HEM(TCNQ)$_2$ crystals was studied by TG–MS (Fig. 6a). The TG curve indicated that the decomposition of HEM(TCNQ)$_2$ undergoes two different steps. The first-step weight loss between 173 and 227 °C is about 12%. From the mass spectrum of evolution products of HEM(TCNQ)$_2$, the curves of ions with the mass-to-

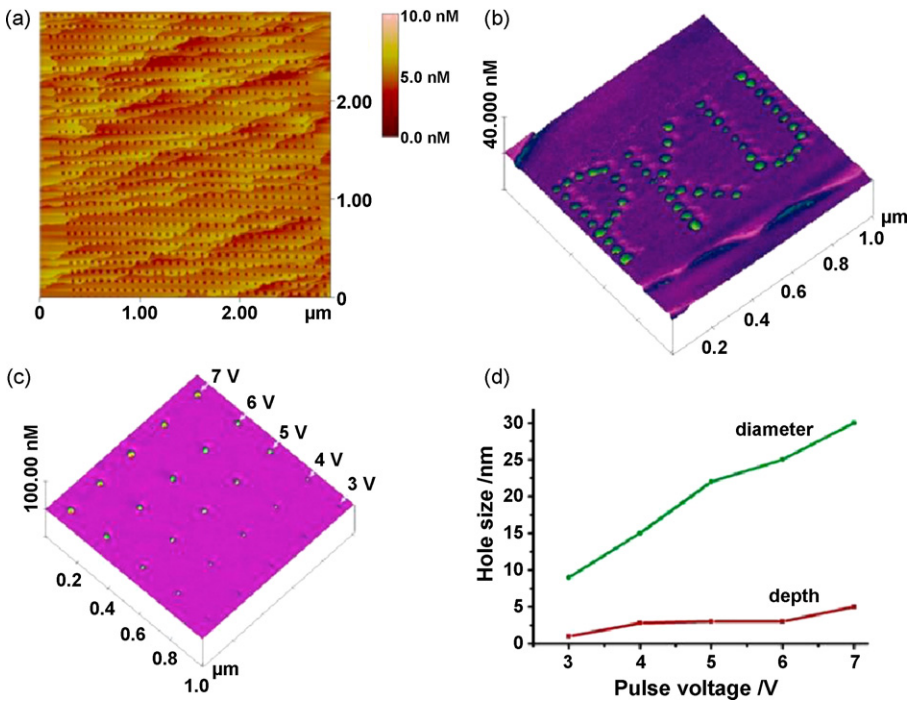

Fig. 7. (a) STM image of a large-scale hole array written on DBA(TCNQ)$_2$ by voltage pulses of 8 V × 300 μs. (b) Nanometer-scale letters written by voltage pulses of 8 V × 300 μs. (c) Dependence of hole size on the pulse voltage. A 5 × 5 array formed by voltage pulses of 3, 4, 5, 6 and 7 V at a fixed duration of 300 ms, respectively. Imaging conditions for (a–c): I_t = 0.10 nA, V_b = 0.10 V, constant-current mode. (d) The size of hole as a function of the pulse voltage. These graphics are reproduced from Ref. [111]. Copyright Wiley–VCH Verlag GmbH & Co. KGaA. Reproduced with permission.

charge ratio (m/z) 12, 13, 14, 26 and 27 amu are observed to peak at the same temperature (~211 °C), which are identified as the cyano group cleaved from TCNQ. In addition, the ion current with m/z 115 amu increases observably at about 227 °C, accompanied by the appearance of the ions with the m/z 29, 42, 56, 57, 70, and 100 amu. The mass spectrum monitored at 273 °C shown in Fig. 6b indicated that all fragment ions with the m/z 29, 42, 56, 57, 70, and 100 amu originate from the same parent-molecule ion, 4-ethylmorpholine (m/z 115). The results of TG–MS experiments show that the possible decomposition mechanism of HEM(TCNQ)$_2$ crystals involves the initial elimination of cyano group of TCNQ moiety by abstracting a proton from the HEM and the subsequent vaporization of the low-boiling point component, 4-Ethylmorpholine (boiling point: 139 °C).

From our extensive TG–MS experiments, a series of ammonium–TCNQ and N-substituted morpholinium–TCNQ CT complexes exhibit a similar thermal decomposition process as follows [114]. The decomposition reaction usually undergoes two different steps. In the first fast step at around 200 °C, the proton of the cation attacks the neighboring CN group of TCNQ moiety, releasing HCN gas and the low-boiling point component of cation. In the second step, the intermediates species generated in the first-step decomposition, releases various low molecular weight species, corresponding to the slower mass loss step. For ternary ammonium–TCNQ–iodide, the decomposition process is more complicated. In addition to the low-boiling point species of the cations and HI released in the first decomposition step, HCN and other volatile alkyl iodine were byproduced. Note that the TCNQ is not directly gasified during the thermal decomposition.

5. Data storage on charge-transfer complexes

5.1. Hole-formation on charge-transfer complexes

THB recording was performed using a computer-controlled program. The STM tip was moved to a desired place, giving a voltage pulse to the tunneling gap while the feedback was turned off. After that, the feedback was switched on and the tip went to another setting place for data writing. Fig. 7a shows a large-area hole array on the *ac*-plane of DBA(TCNQ)$_2$ crystal written by pulses of 8 V (sample vs. tip), applied for 300 μs (8 V × 300 μs pulses). The terraced structure on the crystal surface was also clearly visible. The terraces were consistent with vertical steps of approximately 1.5 nm, nearly equivalent to the *b* lattice parameter of DBA(TCNQ)$_2$. Holes having diameters of 28–35 nm and depths of 4–6 nm were observed on every terrace. The writing reliability reached 100%. This demonstrated that DBA(TCNQ)$_2$ is a suitable hole burning material for STM data storage. With the computer program, a "PKU" pattern can be burnt under the same condition (Fig. 7b). We have also carried out hole-burning experiments on various CT complexes. The writing reliability in all cases can reach 100% with a suitable writing pulse.

The hole size depends on both pulse height and pulse duration. As shown in Fig. 7c and d, the hole size increased in both diameter and depth by increasing the pulse voltage. There exists a threshold voltage for the hole-formation with a fixed pulse duration. In the case of DBA(TCNQ)$_2$, with a fixed pulse duration of 300 μs, no discernible holes were formed when the pulse voltage was below 3 V. In addition, the threshold voltage of the hole-formation strongly depends on the pulse duration [110]. In the case of DPA(TCNQ)$_2$ [DPA = dipropylammonium], a higher threshold voltage needs a shorter pulse duration to create holes on the crystal surface, or vice versa. In the THB process, the thermochemical reaction occurs when the total energy input is large enough to elevate the local temperature to the decomposition temperature of a CT complex. Apparently, the increase of pulse voltage will result in a current increase and thus the increase of total power input. Therefore, the higher pulse voltage needs a shorter pulse duration to induce hole-formation. This dependence of threshold voltage on pulse duration strongly supports the current-related hole-formation mechanism, rather than the electric field-related mechanism [63,110].

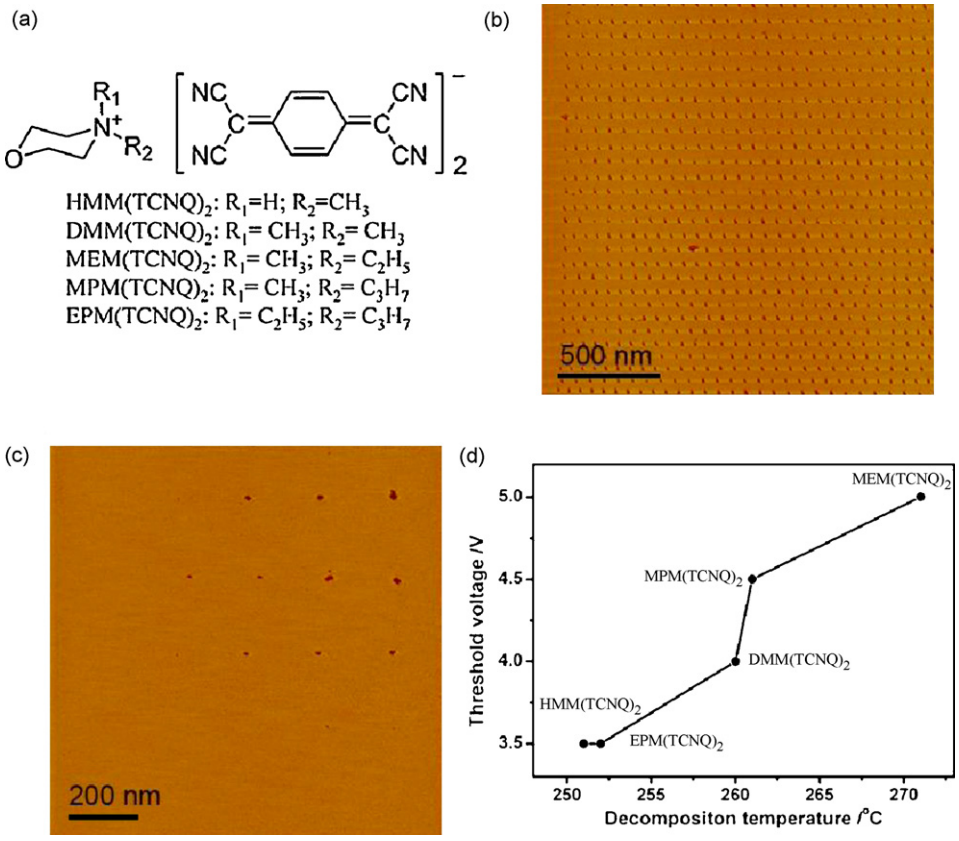

Fig. 8. (a) Molecular structure of N-substituted morpholinium–TCNQ CT complexes. (b) A 28 × 28 hole array burnt on the *ac*-plane of $DMM(TCNQ)_2$ by a voltage pulse of 3 V × 300 μs. (c) Hole array created on $DMM(TCNQ)_2$ at different pulse conditions for obtaining the writing threshold, where the voltage and duration of writing pulse were changed from 3 to 5 V at an interval of 0.5 V (bottom to top), and from 100 to 300 μs at an interval of 50 μs (left to right), respectively. (d) Dependence of threshold voltage at a given pulse duration of 150 μs on the decomposition temperature of N-substituted morpholinium–TCNQ CT complexes, in which the lines connecting data points are only a guide to the eyes. These graphics are reproduced from Ref. [114]. Copyright 2005, American Chemical Society.

5.2. Correlation of hole-burning performance and physicochemical property

As mentioned above, the properties of the storage medium plays a crucial role in the storage performance. In the study of THB storage, we found that the hole burning properties of CT single crystals have a close relationship with their physiochemical properties, such as decomposition temperature, thermal conductivity, and electrical conductivity, which demonstrated the feasibility of molecular design of storage materials in optimizing the hole-burning performance.

5.2.1. Decomposition temperature

The thermogravimetric analysis showed that $DPA(TCNQ)_2$ and $MEM(TCNQ)_2$ begin to decompose at 225 and 271 °C, respectively [110]. In the hole-burning experiments on $DPA(TCNQ)_2$ and $MEM(TCNQ)_2$, we found that the threshold voltage of hole-formation in $MEM(TCNQ)_2$ is much higher than that in $DPA(TCNQ)_2$. We believe that the threshold voltage of hole-formation is related to the decomposition temperature of the CT complex: the higher the decomposition temperature, the larger the writing threshold.

Theoretically [110], a larger energy input would be necessary for hole burning in a CT complex with a higher decomposition temperature. A larger energy input is proportional to a larger pulse voltage with a fixed pulse duration. As a result, the threshold voltage for hole burning is increased with an increase of the decomposition temperature of the CT complex.

In order to investigate this relationship in detail, we have carried out hole-burning experiments on a series of CT complexes, N-substituted morpholinium–TCNQ, as listed in Fig. 8a [114]. Take $DMM(TCNQ)_2$ as an example, Fig. 8b showed a large-area array of holes formed on the $DMM(TCNQ)_2$. The holes have a uniform shape with the diameter of ca. 11 nm and depth of ca. 3 nm. The writing reliability was 100%, suggesting that morpholinium–TCNQ CT complexes are also suitable THB materials. As shown in Fig. 8c, with the decrease of voltage or duration of the writing pulse, the diameters and the depths of the holes showed a gradual decrease. The threshold voltage for hole-formation obtained is ca. 4 V at a 150 μs pulse duration.

To correlate the hole-burning performance with the thermochemical properties of CT complexes, the macroscopic decomposition behavior was studied by TG–MS experiments. As mentioned in Section 4.5, the morpholinium–TCNQ complexes undergo a similar thermochemical decomposition process according to the TG–MS studies. The decomposition temperatures of five morpholinium–TCNQ complexes are determined to be 251, 260, 271, 261, and 252 °C for $HMM(TCNQ)_2$, $DMM(TCNQ)_2$, $MEM(TCNQ)_2$, $MPM(TCNQ)_2$ and $EPM(TCNQ)_2$, respectively. Fig. 8d shows a plot of the threshold voltage vs. the decomposition temperature for all the five N-substituted morpholinium–TCNQ complexes. Unambiguously, higher decomposition temperature corresponds to a larger writing threshold. Similar correlation between decomposition temperature and threshold voltage was observed in a series of alkyl ammonium–TCNQ–iodine CT complexes [113]. The total energy for heating and decomposing the CT complex can be expressed by $E = IV_b t$, where I is the STM current, V_b is the pulse voltage, and t is the pulse duration. Since a series of CT complexes have similar electric resistivities and crystal structures, there would be not much difference in their current–voltage (I–V) relationships. Hence, a large-energy input E is equivalent to a

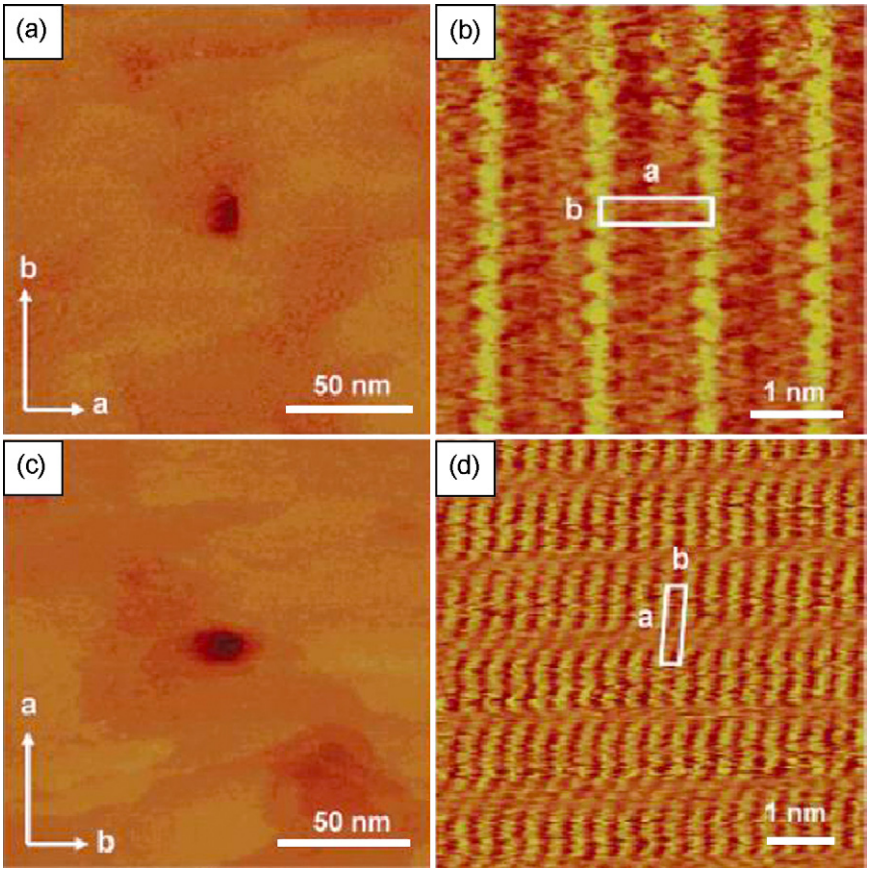

Fig. 9. STM image of a hole written on the *ab*-plane of TTF–TCNQ single crystal by voltage pulses of 5 V × 100 ms (tip negative) before (a) and after (c) rotating the sample by an angle of 90° without any other change, followed by high-resolution STM imaging. Molecular-resolution STM images of the *ab*-plane of TTF–TCNQ single crystal before (b) and after (d) rotation. The measured size of the unit cell in (b) and (d) is 1.25 nm × 0.38 nm, in good agreement with that in the *ab*-plane, 1.2298 nm × 0.3819 nm. The angle between these two directions is ca. 89°, nearly identical to the γ value (90°). Imaging conditions: I_t = 0.10 nA, V_b = 0.10 V, constant-current mode. These graphics are reproduced from Ref. [115]. Copyright 2007, American Chemical Society.

large pulse voltage at a fixed pulse width *t*. Apparently, the threshold voltage for hole-formation is increased with the increase of the decomposition temperature of a CT complex, consistent with the thermochemical-hole-burning process.

5.2.2. Thermal conductivity

The thermal conductivity of a CT complex plays an important role in the THB process. We have observed a remarkably anisotropic THB phenomenon on the tetrathiafulvalene–tetracyanoquinodimethane (TTF–TCNQ) single crystal [115]. TTF–TCNQ is a well-known CT complex as the first organic metal with a large conductivity anisotropy in *ab*-plane. A strong anisotropy of thermal conductivity also exists in the *ab*-plane according to the experimental measurements [119,121] and theoretical analysis [115]. In our hole-burning experiments, an elliptic hole was formed on the *ab*-plane of TTF–TCNQ with the major axis of the ellipse along the high thermal conductivity *b*-axis (Fig. 9).

Considering the rapid lateral thermal diffusion on the surface of CT complex during the THB process, the shape of hole may depends on the thermal conducting property of the CT complex [115]. In the case of TTF–TCNQ, elliptic isothermal region was formed on the crystal surface and those areas where the temperature is above the decomposition point of TTF–TCNQ began to decompose, leaving an elliptic hole on the crystal surface. Similar THB process was carried out on the *bc*-plane of TEA(TCNQ)$_2$ crystal. However, no obvious anisotropic hole burning effect related with the lattice orientation was observed, consistent with the thermal isotropy of the *bc*-plane in TEA(TCNQ)$_2$ [120].

5.2.3. Electrical conductivity

Another important physicochemical property of TCNQ-based CT complexes is electrical conductivity, which is dominated by the structure of the quasi-1D TCNQ chains in crystals. The TCNQ chains can be modulated by the donor molecules in CT complexes, leading to large variations in electrical conductivity. In our various THB storage materials, the difference in the electrical conductivity can exceed six orders of magnitudes [116]. We studied the correlation between the THB behavior and the electrical conductivity, and found that for the low and high electrical conductivity CT complexes, the dependence of hole size on the tip–sample distance exhibits two distinct fashions.

Experimentally, we chose two typical isomorphous quinolinium–TCNQ CT complexes with distinct longitudinal conductivities, PrQ(TCNQ)$_2$ (PrQ = N-propyl-quinolinium; $\sigma_b = 1.5 \times 10^{-2}$ S cm^{-1}) and BuQ(TCNQ)$_2$ (BuQ = N-butyl-quinolinium; $\sigma_b = 1.5 \times 10^{-6}$ S cm^{-1}). For the relatively high conductivity complex, the hole size monotonously decreases with increasing tip–sample distance; however, for the low conductivity complex, the hole size first increases and then decreases with increasing tip–sample distance. We believe that this phenomenon is closely related to the heat dissipation of the metal tip and deformation at the sample surface induced by the strong tip–sample interaction in the case of the low electrical conductivity complex.

These observations provide guidance to optimize the hole writing conditions for improving the storage performance, such as writing reliability and storage density. In particular, for the CT complex storage materials with relatively low electrical conductivity,

by applying the voltage pulse at a large initial tip–sample distance the writing reliability will be significantly improved [116].

6. Effects of tip design on hole-burning performance

6.1. Au-coated W tip

Since the heating effect of STM current is responsible for the hole-formation, the heat conduction of the STM tip plays a role because the tip is either in actual contact or in very close proximity with the sample surface. We commonly use conventional Pt/Ir STM tips for our THB storage. The thermal conductivity of the Pt/Ir metal tip is about 71.6 $W K^{-1} m^{-1}$, usually 2–3 orders of magnitude larger than that of the CT complexes [115]. When applying a voltage pulse, a great amount of heat energy could be transmitted away through the metal tip, which may result in the insufficient heat energy to create a hole.

To confirm the heat conduction effect by STM tips and optimizing the storage performance, recently we have performed a THB experiment on the $TEA(TCNQ)_2$ surface with an Au-coated W tip. The hole size created with the Au-coated W tip was smaller than that obtained with the Pt/Ir tip, under the same writing conditions. For example, under the same pulse condition 8 V × 100 μs, the hole volumes are 7.87×10^3 and 4.72×10^3 nm^3 with a Pt/Ir tip and a Au-coated W tip, respectively. This can not only be explained with the different curvature radius between the Au-coated W tip and Pt/Ir tip, since extensive investigations with the two kinds of tips newly prepared have shown the same phenomena. In addition, the work function of Au (5.4 eV) is almost the same as the work function of Pt/Ir (5.7 eV) [91], while the thermal conductivity of Au (317 $W K^{-1} m^{-1}$) [146] is much higher than that of Pt/Ir (71.6 $W K^{-1} m^{-1}$). Under the same voltage pulse conditions and STM image conditions, the joule heat produced by the two kinds of tips is almost the same, but more heat is lost away from the Au-coated W tip, resulting in smaller holes.

6.2. Single-walled carbon nanotube tip

Carbon nanotube tips represent a breakthrough in scanning probe technology in several regards due to the high aspect ratio, the small tube diameter (~1–2 nm), unique electrical property, and damage resistance resulting from reversible elastic buckling [147–161]. Instead of conventional Pt/Ir STM tips, single-walled carbon nanotube (SWNT) tips prepared by a chemical assembly technique we developed [162] have been used to induce more localized THB process on CT complex, enabling a remarkable improvement in storage density [112].

Theoretically, the thermochemical decomposition of CT complex was induced by the "hot" field-emission electrons since the effective writing voltage exceeds the work function of the tip. It is well known that the geometry of an emitting tip strongly affects the emitting area and the emitting current density. As an ideal nanoemitter [163–165], the SWNT tip can undoubtedly generate more localized field-emission current than the Pt/Ir tip whose typical curvature radius is ca. 60 nm. Since the heating area in field emission is strongly localized around the emitting area [89], the SWNT tip can be employed as promising nanometer-scale heating sources to achieve ultrahigh-density THB storage.

Experimentally, we recently found that the Pt/Ir tip created holes of ca. 25 nm in diameter whereas the SWNT tip gave holes of only ca. 9 nm in diameter under the same pulse condition of 6 V × 100 μs [112]. The storage density could be increased by a factor of 7.7. The smallest hole created with the SWNT tip was about 3 nm in diameter, corresponding to a possible storage density of about 10^{13} bit/in.^{2}.

7. Mechanism

7.1. Theoretical estimation of temperature rise

In our previous work [110,114], we have investigated the heat producing mechanism during the thermochemical-hole-burning process in more detail. Herein, we do not attempt to study the detailed underlying physics, but roughly estimate the temperature rise in the thermochemical-hole-burning process. The maximum temperature rise from STM current heating effect can be estimated from the equation:

$$\Delta T = \frac{\rho J^2 l^2}{2\kappa} \quad (3)$$

where ρ is the electrical resistivity of the sample, J is the current density, l is the length of a cylindrical rod between the highest temperature location and the lowest temperature location, and κ is the sample thermal conductivity [166]. Take TTF–TCNQ for example, the electrical resistivity along c^*-axis, perpendicular to the imaging surface, is 0.2 Ω m. The thermal conductivity has a level of 1 $W m^{-1} K^{-1}$. The current flow between STM tunneling gap was over 120 nA with an osilloscope for a writing pulse of 5 V × 100 μs on the TTF–TCNQ crystal. Supposing that ρ and κ do not change with temperature and no decomposition occurs inside the rod of interest, we obtained the temperature rise, ΔT = 910 °C, for an electron flux of 2 nm in radius and a typical hole depth of l = 10 nm. This roughly estimated value, adding the room temperature of ca. 20 °C, is much higher than the decomposition temperature, 180 °C, of TTF–TCNQ. We concluded that due to the high electrical resistivity and low thermal conductivity of the CT complex, STM current Joule heating effect would be remarkable compared to the decomposition temperature of CT complex and lead to the occurrence of localized thermochemical decomposition of CT complex crystal.

7.2. Experimental evidences for hole-burning mechanism

It is a challenge to clarify experimentally the physical and/or chemical processes in THB because the changes occur on a highly localized area, usually from a few nanometers to tens of nanometers. We have extensively studied the hole-formation mechanism based on some experimental results. AFM imaging after hole-formation confirmed that the holes originate from the morphology change instead of the surface conductance change. The possibility of mechanical indentation was excluded by comparing the STM imaging after thermochemical hole burning with the imaging after direct mechanical writing [111]. Obvious hillocks were observed around the holes created by tip indentation, whereas no hillocks were observed around the holes formed by applying voltage pulses. Holes can also be formed in a high-purity N_2 atmosphere or octanol solution, which indicate that the existence of oxygen or water is not necessary and rule out the possibility of the electrochemical reaction mechanism for hole-formation.

As mentioned above, the threshold voltage of hole-formation depends on the pulse duration [110]. This behavior cannot be interpreted by the field-ion evaporation mechanism [63,65], whereas it strongly supports the current-related mechanism [110]. The hole volume was proportional to the square of the pulse voltage at fixed pulse duration and to the pulse duration at a fixed pulse voltage within a certain time scale, which is consistent with the thermochemical-hole-burning mechanism [110,114]. In addition, both positive and negative voltage pulses can generate the same kind of holes, which excludes the possibility of a tip-induced localized oxidation mechanism. As a negative pulse was applied to the substrate, electrons accelerated across the tunnel gap impacted on the tip. Hence, the possibility of the radiation damage mechanism

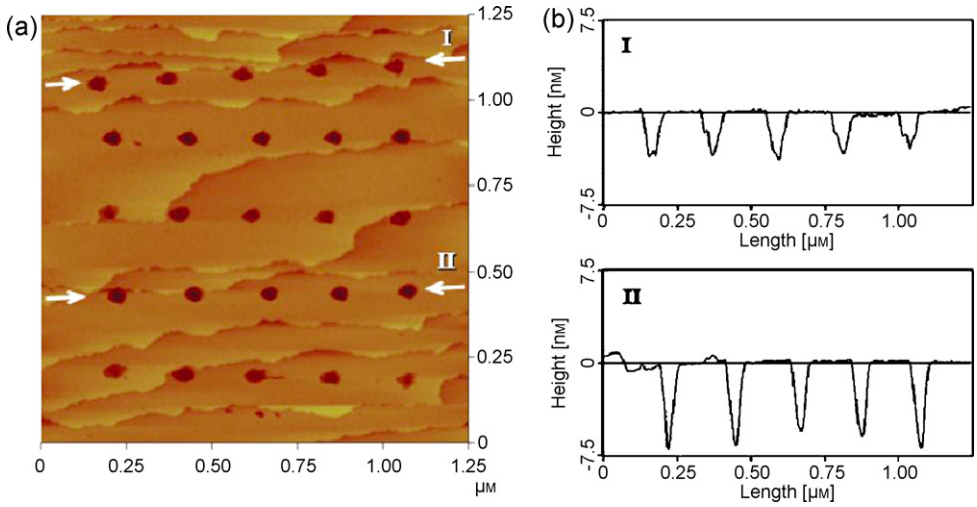

Fig. 10. (a) STM image of a 5 × 5 hole array formed on DBA(TCNQ)$_2$ by voltage pulses of 8, −8, 8, −8 and 8 V at a fixed duration of 300 μs, corresponding to rows from bottom to top, respectively. Imaging conditions: I_t = 0.10 nA, V_b = 0.10 V, constant-current mode. (b) Cross-section of holes written by pulses of 8 V × 300 μs (I) and −8 V × 300 μs (II), indicated by the arrows in (a).

for hole-formation, i.e. the bond rupture of the substrate by direct electron excitation [167], is also ruled out.

The measured depth of the same burnt hole was dependent on the imaging-bias polarity. In contrast, the measured depth of the mechanically created hole showed no difference with different voltage polarities. The phenomenon of bias-dependent contrast in STM imaging of the burnt hole, reflecting the different electronic states involved in the tunneling process [132,168], suggesting that the chemical species inside the holes are different from the surroundings, i.e. the occurrence of chemical reactions of CT complexes in the THB process. The residual TCNQ moieties might be left in the hole after thermochemical decomposition of CT complex, as described previously in Sections 4.4 and 4.5. A hole-trapped area having lower electron density might be formed in the vicinity of electron acceptors TCNQ. Therefore, in the STM imaging, an electron flowed from the hole region to STM tip (tip positive) resulted in a less bright STM image than the reverse case. In other words, the depth of holes appeared differently with different imaging-bias polarities. This phenomenon strongly supports the THB mechanism.

The polarity of the applied voltage pulse affects the depth of the hole formed on various CT complexes. Generally, applying a negative pulse can create a deeper hole than a positive pulse. Take the DBA(TCNQ)$_2$ for example, apparently, both positive and negative voltage pulses formed the same kind of holes (Fig. 10a). However, the depth of holes formed by applying negative pulses of −8 V × 300 μs was ca. 7 nm, remarkably larger than the depth (ca. 4.0 nm) of holes in the positively pulsed case (Fig. 10b).

Theoretically, one cannot wholly neglect the influence of the field-induced diffusion and evaporation of the adsorbed atoms and molecules on substrate surface within the region beneath the tip, which often occurred under a high electric field [65,169]. In the negatively pulsed case, the situation became more complicated as the possibility arose for field-induced evaporation of negative species from the substrate. Thus, accompanied with the thermal decomposition of DBA(TCNQ)$_2$ induced by an STM current heating effect, negative species, such as residual $TCNQ^-$ moieties near the hole, might be dragged from the substrate to the positive tip across the substrate-tip gap, which caused a remarkable increase of hole depth as compared with the positively pulsed case.

The reliability for hole-formation, which is one of the critical parameters for a practical storage technique, strongly depends on the bias polarity of writing pulses. Although both positive and negative writing pulses could generate nanoscale holes on CT complexes, higher hole-formation probability was usually achieved when the STM tip was negatively biased. Possible mechanism for this bias polarity-dependent thermochemical-hole-burning effect was discussed in the case of HEM(TCNQ)$_2$ [HEM = 4-ethylmorpholinium]. As mentioned above, the dependence of hole burning performance on the writing tips is in relation to the features of writing electron beams [112]. When the tip was negatively biased, filed emission current that flowed through the sharpest apex section of the tip could heat up the tip apex region and even melt as the current density was high enough [61,170]. A temperature and field-gradient-induced surface atom diffusion from tip shank to the apex could result in sharpening the tip [64]. The current density from a relatively small area of the sharpened tip apex is high and stable, which would achieve nanometer-scale hole-formation with high writing probability on the sample surface. If the tip was positively pulsed, on the other hand, the electron was field emitted from the "blunt" sample surface. A diffused electron beam was generated to impinge the tip over a relatively large area [64]. Therefore, the heating effect of diffused current might result in relatively low writing probability.

7.3. Hole-burning in UHV-VT system

To provide direct evidence of the thermochemical reaction mechanism induced by STM current joule heating, we have performed the THB experiment with TEA(TCNQ)$_2$ in an ultrahigh vacuum system (UHV) with a variable temperature STM (VT-STM) [117]. The THB behavior in the UHV system was similar to those under ambient conditions, except that the average hole diameter became larger, which was presumably attributed to fewer conduction paths of heat energy in the UHV system. Our THB experiments in the UHV system strictly excluded the possibility of the local oxidation mechanism that often occurred under humid conditions because oxygen and water were absent.

In principle, the change of the specimen temperature has no influence on the hole if the hole-formation is induced by the electric field evaporation and the electron bombardment. On the contrary, the local heating effect, which leads to the thermal decomposition of the specimen, is directly correlated to the change of the specimen temperatures. More heat energy input will be required

to reach the decomposition temperature point if the specimen is cooled below room temperature. That is, the hole should be created under a larger pulse voltage and current. By varying the specimen temperature from room temperature to 215 K in our UHV-VT system, we found that the threshold voltage of the hole-formation on TEA(TCNQ)$_2$ is highly temperature-dependent. Threshold voltage of hole-formation increased and volumes of the holes became smaller as the specimen temperatures are reduced. These observations might give a direct correlation between the decomposition reaction and the joule heat induced by STM current, therefore strongly supporting the THB mechanism.

8. Conclusions

An overview of recent advances in SPM-based data storage techniques is presented. Representative achievements have been highlighted from the viewpoints of recording principles including electrical bistability, photoelectrochemical conversion, field-induced charge storage, atomic manipulation or deposition, localized oxidation, magneto-optical or magnetic recording, thermally induced physical deformation or phase change, and so forth. In addition, great efforts have been made to improve the data rate that is the long-time concern in SPM-based data storage. The ceaseless emergence of new data storage principle that combines high density and high performance would finally provide a practical next-generation data storage system.

As a novel SPM-based data storage technique, a thermochemical-hole-burning technique was developed in our group. We have mainly summarized our recent achievements in design and synthesis of organic CT complexes towards thermochemical-hole-burning memory, the correlation between hole-burning performances and physicochemical properties of CT complexes, the STM tip design and its effects on the hole-burning performance, as well as the storage mechanism.

We have developed thirty THB storage materials, including several series of TCNQ-based complexes—ammonium–TCNQ, quinoline–TCNQ, pyridine–TCNQ, morpholinium–TCNQ, and ternary ammonium–TCNQ–iodide. The information bit was recorded as a nanometer-sized burnt hole, and we have achieved about 1 Tbit/in.^{2} storage density using single-walled carbon nanotube STM tips. Our systematic studies on the correlation of hole-burning performance and phyisochemsical properties of the CT complexes provide further molecular design rules of CT complexes towards optimizing the storage performance. The mechanism of hole-formation has also been extensively studied, which strongly supports the localized thermochemical reaction mechanism induced by STM current joule heating. The thermochemical-hole-burning process involves energy conversion and dissipation, heat transfer and chemical reaction, which provides a nanoreactor model for investigating localized physicochemical properties and the kinetics and thermodynamics of nanometer-scale reactions.

Acknowledgements

We would like to thank Xiaoming Huang, Chunbo Ran, Wei Zhou, Liang Ren, Stefan Meister for the helpful discussion. This work was supported by the National Natural Science Foundation of China (Grants 50821061, 20833001, 20973013, 20973007) and Ministry of Science and Technology of China (Grants 2007CB936203, 2006CB932403).

References

[1] G. Binning, H. Rohrer, Helv. Phys. Acta 55 (1982) 726.
[2] G. Binning, H. Rohrer, C. Gerber, E. Weibel, Phys. Rev. Lett. 49 (1982) 57.
[3] G. Binning, H. Rohrer, C. Gerber, E. Weibel, Phys. Rev. Lett. 50 (1983) 120.
[4] G. Binning, C.F. Quate, C. Gerber, Phys. Rev. Lett. 56 (1986) 930.
[5] D.W. Abraham, F.A. McDonald, Appl. Phys. Lett. 56 (1990) 1181.
[6] J.J. Saenz, N. Garcia, P. Grutter, E. Meyer, H. Heinzelmann, R. Wiesendanger, L. Rosenthaler, H.R. Hidber, H.J. Guntherodt, J. Appl. Phys. 62 (1987) 4293.
[7] A. Lewis, M. Isaacson, A. Harootunian, A. Muray, Ultramicroscopy 13 (1984) 227.
[8] E. Betzig, J.K. Trautman, R. Wolfe, E.M. Gyorgy, P.L. Finn, M.H. Kryder, C.H. Chang, Appl. Phys. Lett. 61 (1992) 142.
[9] R. Garcia, R.V. Martinez, J. Martinez, Chem. Soc. Rev. 35 (2006) 29.
[10] R.M. Nyffenegger, R.M. Penner, Chem. Rev. 97 (1997) 1195.
[11] Y. Yang, J. Ouyang, L. Ma, R.J.-H. Tseng, C.-W. Chu, Adv. Funct. Mater. 16 (2006) 1001.
[12] G. Jiang, Y. Song, X. Guo, D. Zhang, D. Zhu, Adv. Mater. 20 (2008) 2888.
[13] D.M. Eigler, E.K. Schweizer, Nature 344 (1990) 524.
[14] Z.F. Liu, K. Hashimoto, A. Fujishima, Nature 347 (1990) 658.
[15] R.C. Barrett, C.F. Quate, J. Appl. Phys. 70 (1991) 2725.
[16] H.J. Mamin, D. Rugar, Appl. Phys. Lett. 61 (1992) 1003.
[17] B.W. Chui, T.D. Stowe, T.W. Kenny, H.J. Mamin, B.D. Terris, D. Rugar, Appl. Phys. Lett. 69 (1996) 2767.
[18] H.J. Mamin, Appl. Phys. Lett. 69 (1996) 433.
[19] C. Liu, H. Pan, M.A. Fox, A.J. Bard, Science 261 (1993) 897.
[20] A. Sato, Y. Tsukamoto, Nature 263 (1993) 431.
[21] A. Sato, S. Momose, Y. Tsukamoto, J. Vac. Sci. Technol. B 13 (1995) 2832.
[22] H. Kado, T. Tohda, Appl. Phys. Lett. 66 (1995) 2961.
[23] K. Yano, T. Ikeda, Appl. Phys. Lett. 80 (2002) 1067.
[24] K. Yano, M. Kyogaku, R. Kuroda, Y. Shimada, S. Shido, H. Matsuda, K. Takimoto, O. Albrecht, K. Eguchi, T. Nakagiri, Appl. Phys. Lett. 68 (1996) 188.
[25] L.P. Ma, W.J. Yang, Z.Q. Xue, S.J. Pang, Appl. Phys. Lett. 73 (1998) 850.
[26] L.P. Ma, Y.L. Song, H.J. Gao, W.B. Zhao, H.Y. Chen, Z.Q. Xue, S.J. Pang, Appl. Phys. Lett. 69 (1996) 3752.
[27] H.J. Gao, L.P. Ma, H.X. Zhang, H.Y. Chen, Z.Q. Xue, S.J. Pang, J. Vac. Sci. Technol. B 15 (1997) 1581.
[28] E.B. Cooper, S.R. Manalis, H. Fang, H. Dai, K. Matsumoto, S.C. Minne, T. Hunt, C.F. Quate, Appl. Phys. Lett. 75 (1999) 3566.
[29] X.X. Bao, H.F. Chen, Z.F. Liu, Nanometer-scale fabrication and data storage on charge transfer complex TEA (TCNQ)(2) single crystal, in: J.W. Perry, A. Scherer (Eds.), Micro- and Nano-Photonic Materials and Devices, Spie-Int Soc Optical Engineering, Bellingham, 2000, p. 172.
[30] M.I. Lutwyche, M. Despont, U. Drechsler, U. Dürig, W. Häberle, H. Rothuizen, R. Stutz, R. Widmer, G.K. Binnig, P. Vettiger, Appl. Phys. Lett. 77 (2000) 3299.
[31] U.J. Quaade, K. Stokbro, R. Lin, F. Grey, Nanotechnology 12 (2001) 265.
[32] M. Cavallini, F. Biscarini, S. León, F. Zerbetto, G. Bottari, D.A. Leigh, Science 299 (2003) 531.
[33] H.F. Hamann, M. O'Boyle, Y.C. Martin, M. Rooks, H.K. Wickramasinghe, Nat. Mater. 5 (2006) 383.
[34] A. Jo, W. Joo, W.-H. Jin, H. Nam, J.K. Kim, Nat. Nanotechnol. 4 (2009) 727.
[35] L.P. Ma, J. Liu, Y. Yang, Appl. Phys. Lett. 80 (2002) 2997.
[36] H.M. Wu, Y.L. Song, S.X. Du, H.W. Liu, H.J. Gao, L. Jiang, D.B. Zhu, Adv. Mater. 15 (2003) 1925.
[37] D.X. Shi, Y.L. Song, D.B. Zhu, H.X. Zhang, S.H. Xie, S.J. Pang, H.J. Gao, Adv. Mater. 13 (2001) 1103.
[38] D.X. Shi, Y.L. Song, H.X. Zhang, P. Jiang, S.T. He, S.S. Xie, S.J. Pang, H.J. Gao, Appl. Phys. Lett. 77 (2000) 3203.
[39] Y.L. Shang, Y.Q. Wen, S.L. Li, S.X. Du, X.B. He, L. Cai, Y.F. Li, L.M. Yang, H.J. Gao, Y. Song, J. Am. Chem. Soc. 129 (2007) 11674.
[40] J.C. Li, Z.Q. Xue, K.Z. Wang, Z.M. Wang, C.H. Yan, Y.L. Song, L. Jiang, D.B. Zhu, J. Phys. Chem. B 108 (2004) 19348.
[41] J.C. Li, Z.Q. Xue, X.L. Li, W.M. Liu, S.M. Hou, Y.L. Song, L. Jiang, D.B. Zhu, X.X. Bao, Z.F. Liu, Appl. Phys. Lett. 76 (2000) 2532.
[42] H.J. Gao, K. Sohlberg, Z.Q. Xue, H.Y. Chen, S.M. Hou, L.P. Ma, X.W. Fang, S.J. Pang, S.J. Pennycook, Phys. Rev. Lett. 84 (2000) 1780.
[43] Z.H. Cheng, L. Gao, Z.T. Deng, N. Jiang, Q. Liu, D.X. Shi, S.X. Du, H.M. Guo, H.J. Gao, J. Phys. Chem. C 111 (2007) 9240.
[44] L. Cai, M. Feng, H.M. Guo, W. Ji, S.X. Du, L.F. Chi, H. Fuchs, H. Gao, J. Phys. Chem. C 112 (2008) 17038.
[45] F.M. Raymo, Adv. Mater. 14 (2002) 401.
[46] S.R. Ovshinsky, Phys. Rev. Lett. 21 (1968) 1450.
[47] H. Fritzsche, S.R. Ovshinsky, J. Non-Cryst. Solids 2 (1970) 393.
[48] R. Pandian, B.J. Kooi, G. Palasantzas, J.T.M. De Hosson, A. Pauza, Adv. Mater. 19 (2007) 4431.
[49] F.M. Schellenberg, W. Lenth, B.C. Bjorklund, Appl. Opt. 25 (1986) 3207.
[50] J. Friedrich, D. Haarer, Angew. Chem. Int. Ed. 23 (1984) 113.
[51] C.Y. Liu, A.J. Bard, Acc. Chem. Res. 32 (1999) 235.
[52] Y. Ma, Y.Q. Wen, J.X. Wang, Y.L. Shang, S.X. Du, L.D. Pan, G. Li, L.M. Yang, H.J. Gao, Y.L. Song, J. Phys. Chem. C 113 (2009) 8548.
[53] M.S. Suh, C.S. Lee, S.H. Kim, K.I. Lee, J.W. Cho, Y. Kuk, J.K. Shin, Sens. Actuator A: Phys. 136 (2007) 597.
[54] P. Mesquida, H.F. Knapp, A. Stemmer, Surf. Interface Anal. 33 (2002) 159.
[55] X.Q. Chen, H. Yamada, T. Horiuchi, K. Matsushige, S. Watanabe, M. Kawai, P.S. Weiss, J. Vac. Sci. Technol. B 17 (1999) 1930.
[56] A.J. Heinrich, C.P. Lutz, J.A. Gupta, D.M. Eigler, Science 298 (2002) 1381.
[57] M.T. Cuberes, R.R. Schlittler, J.K. Gimzewski, Appl. Phys. Lett. 69 (1996) 3016.
[58] R. Bennewitz, J.N. Crain, A. Kirakosian, J.L. Lin, J.L. McChesney, D.Y. Petrovykh, F.J. Himpsel, Nanotechnology 13 (2002) 499.

[59] J.I. Pascual, J. Mendez, J. Gomez-Herrero, A.M. Baro, N. Garcia, V.T. Binh, Phys. Rev. Lett. 72 (1994) 1129.
[60] J.I. Pascual, J. Mendez, J. Gomez-Herrero, A.M. Baro, N. Garcia, V.T. Binh, Phys. Rev. Lett. 71 (1993) 1852.
[61] U. Gratzke, G. Simon, Phys. Rev. B 52 (1995) 8535.
[62] H.J. Mamin, P.H. Guethner, D. Rugar, Phys. Rev. Lett. 65 (1990) 2418.
[63] T.T. Tsong, Phys. Rev. B 44 (1991) 13703.
[64] C.S. Chang, W.B. Su, T.T. Tsong, Phys. Rev. Lett. 72 (1994) 574.
[65] P.A. Campbell, G.A. Farnan, D.G. Walmsley, Nanotechnology 13 (2002) 69.
[66] S. Kondo, S. Heike, M. Lutwyche, Y. Wada, J. Appl. Phys. 78 (1995) 155.
[67] H. Koyanagi, S. Hosaka, R. Imura, M. Shirai, Appl. Phys. Lett. 67 (1995) 2609.
[68] S. Hosaka, H. Koyanagi, A. Kikukawa, Jpn. J. Appl. Phys. 32 (1993) L464.
[69] J.Q. Song, Z.F. Liu, C.Z. Li, H.F. Chen, H.X. He, Appl. Phys. A 66 (1998) S715.
[70] S. Hosaka, H. Koyanagi, Jpn. J. Appl. Phys. 33 (1994) L1358.
[71] S.C. Eagle, G.K. Fedder, Appl. Phys. Lett. 74 (1999) 3902.
[72] H. Sugimura, T. Uchida, N. Kitamura, H. Masuhara, J. Phys. Chem. 98 (1994) 4352.
[73] H. Sugimura, T. Uchida, N. Kitamura, H. Masuhara, Jpn. J. Appl. Phys. 32 (1993) L553.
[74] H. Sugimura, T. Uchida, N. Kitamura, H. Masuhara, Appl. Phys. Lett. 63 (1993) 1288.
[75] S. Hosaka, H. Koyanagi, A. Kikukawa, M. Miyamoto, I. Ryo, J. Ushiyama, J. Vac. Sci. Technol. B 13 (1995) 1307.
[76] C. Haginoya, K. Koike, Y. Hirayama, J. Yamamoto, M. Ishibashi, O. Kitakami, Y. Shimada, Appl. Phys. Lett. 75 (1999) 3159.
[77] H.F. Hamann, Y.C. Martin, H.K. Wickramasinghe, Appl. Phys. Lett. 84 (2004) 810.
[78] T. Onoue, M.H. Siekman, L. Abelmann, J.C. Lodder, J. Magn. Magn. Mater. 287 (2005) 501.
[79] Y.F. Lu, Z.H. Mai, Y.W. Zheng, W.D. Song, Appl. Phys. Lett. 76 (2000) 1200.
[80] T.D. Milster, Proc. IEEE 88 (2000) 1480.
[81] S. Hosaka, T. Shintani, M. Miyamoto, A. Hirotsune, M. Terao, M. Yoshida, K. Fujita, S. Kammer, Jpn. J. Appl. Phys. 35 (1996) 443.
[82] S. Hosaka, T. Shintani, M. Miyamoto, A. Hirotsune, M. Terao, M. Yoshida, S. Honma, S. Kämmer, Thin Solid Films 273 (1996) 122.
[83] S. Hosaka, A. Kikukawa, H. Koyanagi, T. Shintani, M. Miyamoto, K. Nakamura, K. Etoh, Nanotechnology 8 (1997) A58.
[84] Y. Martin, S. Rishton, H.K. Wickramasinghe, Appl. Phys. Lett. 71 (1997) 1.
[85] J.E. Persson, Solid State Commun. 57 (1986) 769.
[86] B.N.J. Persson, A. Baratoff, Phys. Rev. Lett. 59 (1987) 339.
[87] F. Flores, P.M. Echenique, R.H. Ritchie, Phys. Rev. B 34 (1986) 2899.
[88] J. Nakamura, M. Miyamoto, S. Hosaka, H. Koyanagi, J. Appl. Phys. 77 (1995) 779.
[89] J.B. Xu, K. Läuger, R. Möller, K. Dransfeld, I.H. Wilson, Appl. Phys. A 59 (1994) 155.
[90] T.C. Shen, C. Wang, G.C. Abeln, J.R. Tucker, J.W. Lyding, P. Avouris, R.E. Walkup, Science 268 (1995) 1590.
[91] C.J. Chen, Introduction to Scanning Tunneling Microscopy, 1st ed., Oxford University Press, Oxford, UK, 1993.
[92] S. Alavi, R. Rousseau, S.N. Patitsas, G.P. Lopinski, R.A. Wolkow, T. Seideman, Phys. Rev. Lett. 85 (2000) 5372.
[93] B.C. Stipe, M.A. Rezaei, W. Ho, S. Gao, M. Persson, B.I. Lundqvist, Phys. Rev. Lett. 78 (1997) 4410.
[94] B.C. Stipe, M.A. Rezaei, W. Ho, Science 279 (1998) 1907.
[95] B.C. Stipe, M.A. Rezaei, W. Ho, Phys. Rev. Lett. 82 (1999) 1724.
[96] P.F. Marella, R.F. Pease, Appl. Phys. Lett. 55 (1989) 2366.
[97] D. Saluel, J. Daval, B. Béchevet, C. Germain, B. Valon, J. Magn. Magn. Mater. 193 (1999) 488.
[98] E.I. Altman, D.P. DiLella, J. Ibe, K. Lee, R.J. Colton, Rev. Sci. Instrum. 64 (1993) 1239.
[99] L. Kuipers, R.W.M. Loos, H. Neerings, J. Ter Horst, G.J. Ruwiel, A.P. De Jongh, J.W.M. Frenken, Rev. Sci. Instrum. 66 (1995) 4557.
[100] G. Binnig, M. Despont, U. Drechsler, W.W. Häerle, M. Lutwyche, P. Vettiger, H.J. Mamin, B.W. Chui, T.W. Kenny, Appl. Phys. Lett. 74 (1999) 1329.
[101] H.J. Mamin, R.P. Ried, B.D. Terris, D. Rugar, Proc. IEEE 87 (1999) 1014.
[102] S.C. Minne, S.R. Manalis, C.F. Quate, Appl. Phys. Lett. 67 (1995) 3918.
[103] S.R. Manalis, S.C. Minne, C.F. Quate, Appl. Phys. Lett. 68 (1996) 871.
[104] S.C. Minne, S.R. Manalis, C.F. Quate, Bringing Scanning Probe Microscopy up to Speed, Kluwer Academic Publishers, 1999.
[105] S.C. Minne, S.R. Manalis, A. Atalar, C.F. Quate, J. Vac. Sci. Technol. B 14 (1996) 2456.
[106] G. Binnig, Talk Presented at the 9th Int. Conf. STM'97, Hamburg, Germany, 1997.
[107] P. Vettiger, G. Cross, M. Despont, U. Drechsler, U. Durig, B. Gotsmann, W. Haberle, M. Lantz, H.E. Rothuizen, R. Stutz, IEEE Trans. Nanotechnol. 1 (2002) 39.
[108] P. Vettiger, M. Despont, U. Drechsler, U. Durig, W. Haberle, M.I. Lutwyche, H.E. Rothuizen, R. Stutz, R. Widmer, G.K. Binnig, IBM J. Res. Dev. 44 (2000) 323.
[109] E. Eleftheriou, T. Antonakopoulos, G.K. Binnig, G. Cherubini, M. Despont, A. Dholakia, U. Durig, M.A. Lantz, H. Pozidis, H.E. Rothuizen, IEEE Trans. Magn. 39 (2003) 938.
[110] X.C. Yu, R. Zhang, H.L. Peng, C.B. Ran, Y.Y. Zhang, Z.F. Liu, J. Phys. Chem. B 108 (2004) 14800.
[111] H.L. Peng, C.B. Ran, X.C. Yu, R. Zhang, Z.F. Liu, Adv. Mater. 17 (2005) 459.
[112] H.L. Peng, Z. Chen, L.M. Tong, X.C. Yu, C.B. Ran, Z.F. Liu, J. Phys. Chem. B 109 (2005) 3526.
[113] X.C. Yu, H.L. Peng, C.B. Ran, L. Sun, R. Zhang, Z.F. Liu, Appl. Phys. Lett. 86 (2005) 133105.
[114] C. Ran, H. Peng, W. Zhou, X. Yu, Z. Liu, J. Phys. Chem. B 109 (2005) 22486.
[115] C.B. Ran, H.L. Peng, L. Ren, W. Zhou, Y.D. Ling, Z.F. Liu, J. Phys. Chem. C 111 (2007) 631.
[116] W. Zhou, F. Lin, L. Ren, X.M. Huang, C.B. Ran, S.A. Ding, H.L. Peng, Z.F. Liu, Nanotechnology 19 (2008).
[117] X.M. Huang, F. Lin, W. Zhou, L. Ren, H.L. Peng, Z.F. Liu, J. Phys. Chem. C 112 (2008) 2004.
[118] H.L. Peng, C.B. Ran, Z.F. Liu, Y.Z. Long, Z.M. Wang, Z.Q. Yu, H.L. Sun, Y.G. Wei, S. Gao, Z.J. Chen, E.Q. Chen, J. Phys. Chem. C 112 (2008) 11001.
[119] M.B. Salamon, J.W. Bray, G. DePasquali, R.A. Craven, G. Stucky, A. Schultz, Phys. Rev. B 11 (1975) 619.
[120] H. Grassi, A. Brau, J.P. Farges, Phys. Stat. Sol. B 112 (1982) 633.
[121] M. Kaveh, H. Gutfreund, M. Weger, Phys. Rev. B 20 (1979) 543.
[122] L.R. Melby, R.J. Harder, W.R. Hertler, W. Mahler, R.E. Benson, W.E. Mochel, J. Am. Chem. Soc. 84 (1962) 3374.
[123] M.A. Abkowitz, A.J. Epstein, C.H. Griffiths, J.S. Miller, M.L. Slade, J. Am. Chem. Soc. 99 (1977) 5304.
[124] M. Weger, K. Bender, T. Klutz, D. Schweitzer, F. Gross, C.P. Heidmann, C. Probst, K. Andres, Synth. Met. 25 (1988) 49.
[125] A. Cougrand, S. Fiandrois, P. Delhaes, P. Dupuis, D. Chasseau, J. Galtier, J.L. Miane, Mol. Cryst. Liq. Cryst. 32 (1976) 165.
[126] P. Dupuis, S. Flandrois, P. Delhaes, C. Coulon, J. Chem. Soc. Chem. Commun. (1978) 337.
[127] C. Coulon, S. Flandrois, P. Delhaes, C. Hauw, P. Dupuis, Phys. Rev. B 23 (1981) 2850.
[128] M. Izumi, Y. Kajita, T. Iwazumi, T. Sekine, R.M. Lequan, M. Lequan, Synth. Met. 27 (1988) 257.
[129] K. Xiao, I.N. Ivanov, A.A. Puretzky, Z. Liu, D.B. Geohegan, Adv. Mater. 18 (2006) 2184.
[130] E. Coronado, P. Day, Chem. Rev. 104 (2004) 5419.
[131] C.A. Di, G. Yu, Y.Q. Liu, X.J. Xu, D.C. Wei, Y.B. Song, Y.M. Sun, Y. Wang, D.B. Zhu, J. Liu, X.Y. Liu, D.X. Wu, J. Am. Chem. Soc. 128 (2006) 16418.
[132] S.N. Magonov, M.H. Whangbo, Surface Analysis with STM and AFM: Experimental and Theoretical Aspects of Image Analysis, VCH Weinheim, 1996.
[133] F. Lin, W. Zhou, X.M. Huang, L. Ren, Z.F. Liu, J. Phys. Chem. C 112 (2008) 1090.
[134] A. Girlando, C. Pecile, Spectrochim. Acta A A29 (1973) 1859.
[135] S. Matsuzaki, R. Kuwata, K. Toyoda, Solid State Commun. 33 (1980) 403.
[136] Y. Okimoto, R. Kumai, E. Saitoh, M. Izumi, S. Horiuchi, Y. Tokura, Phys. Rev. B 70 (2004) 115104.
[137] E.I. Kamitsos, W.M. Risen, J. Chem. Phys. 79 (1983) 5808.
[138] E.I. Kamitsos, C.H. Tzinis, W.M. Risen, Solid State Commun. 42 (1982) 561.
[139] K. Ikegami, K. Ono, J. Togo, T. Wakabayashi, Y. Ishige, H. Matsuzaki, H. Kishida, H. Okamoto, Phys. Rev. B 76 (2007).
[140] A.D. Bandrauk, K.D. Truong, C. Carlone, S. Jandl, K. Ishii, J. Phys. Chem. 89 (1985) 434.
[141] K.D. Truong, C. Carlone, Phys. Rev. B 20 (1979) 2238.
[142] J. Wu, Ž. Tomović, V. Enkelmann, K. Müllen, J. Org. Chem. 69 (2004) 5179.
[143] C.N. McEwen, M.A. Rudat, J. Am. Chem. Soc. 101 (1979) 6470.
[144] C.N. McEwen, M.A. Rudat, J. Am. Chem. Soc. 103 (1981) 4343.
[145] M.A. Rudat, C.N. McEwen, J. Am. Chem. Soc. 103 (1981) 4349.
[146] C. Kittel, Introduction to Solid State Physics, 8th ed., John Wiley & Sons, Inc., 2005.
[147] L. Chen, C.L. Cheung, P.D. Ashby, C.M. Lieber, Nano Lett. 4 (2004) 1725.
[148] C.L. Cheung, J.H. Hafner, T.W. Odom, K. Kim, C.M. Lieber, Appl. Phys. Lett. 76 (2000) 3136.
[149] H.J. Dai, Surf. Sci. 500 (2002) 218.
[150] J.H. Hafner, C.L. Cheung, C.M. Lieber, J. Am. Chem. Soc. 121 (1999) 9750.
[151] J.H. Hafner, C.L. Cheung, C.M. Lieber, Nature 398 (1999) 761.
[152] J.H. Hafner, C.L. Cheung, T.H. Oosterkamp, C.M. Lieber, J. Phys. Chem. B 105 (2001) 743.
[153] J.H. Hafner, C.L. Cheung, A.T. Woolley, C.M. Lieber, Prog. Biophys. Mol. Biol. 77 (2001) 73.
[154] C.V. Nguyen, Q. Ye, M. Meyyappan, Meas. Sci. Technol. 16 (2005) 2138.
[155] H. Nishijima, S. Kamo, S. Akita, Y. Nakayama, K.I. Hohmura, S.H. Yoshimura, K. Takeyasu, Appl. Phys. Lett. 74 (1999) 4061.
[156] T. Nishino, T. Ito, Y. Umezawa, Anal. Chem. 74 (2002) 4275.
[157] L.A. Wade, I.R. Shapiro, Z. Ma, S.R. Quake, C.P. Collier, Nano Lett. 4 (2004) 725.
[158] S.S. Wong, J.D. Harper, P.T. Lansbury Jr., C.M. Lieber, Annu. Rev. Mater. Sci. 27 (1997) 381.
[159] S.S. Wong, E. Joselevich, A.T. Woolley, C.L. Cheung, C.M. Lieber, Nature 394 (1998) 52.
[160] S.S. Wong, A.T. Woolley, E. Joselevich, C.L. Cheung, C.M. Lieber, Nature 384 (1996) 147.
[161] S.S. Wong, A.T. Woolley, T.W. Odom, J.L. Huang, P. Kim, D.V. Vezenov, C.M. Lieber, Appl. Phys. Lett. 73 (1998) 3465.
[162] Z. Liu, Z. Shen, T. Zhu, S. Hou, L. Ying, Z. Shi, Z. Gu, Langmuir 16 (2000) 3569.
[163] K. Matsumoto, S. Kinosita, Y. Gotoh, T. Uchiyama, S. Manalis, C. Quate, Appl. Phys. Lett. 78 (2001) 539.

[164] M.A. Guillorn, A.V. Melechko, V.I. Merkulov, E.D. Ellis, C.L. Britton, M.L. Simpson, D.H. Lowndes, L.R. Baylor, Appl. Phys. Lett. 79 (2001) 3506.
[165] O.J. Lee, K.H. Lee, Appl. Phys. Lett. 82 (2003) 3770.
[166] W.W. Dolan, W.P. Dyke, J.K. Trolan, Phys. Rev. 91 (1953) 1054.
[167] L. Reimer, A. Schmidt, Scanning 7 (1985) 47.
[168] A. Miura, Z. Chen, H. Uji-i, S. De Feyter, M. Zdanowska, P. Jonkheijm, A. Schenning, E.W. Meijer, F. Wurthner, F.C. De Schryver, J. Am. Chem. Soc. 125 (2003) 14968.
[169] L.J. Whitman, J.A. Stroscio, R.A. Dragoset, R.J. Celotta, Science 251 (1991) 1206.
[170] N.M. Miskovsy, S.H. Park, J. He, P.H. Culter, J. Vac. Sci. Technol. B 11 (1993) 366.